Performance prediction of a hydrofoil near the free surface using low (BEM) and high (RANS) fidelity methods

Paolo Perali, Matthieu Sacher, Jean-Baptiste Leroux, Jeroen Wackers, Benoît Augier, Frédéric Hauville, Patrick Bot

Performance prediction of a hydrofoil near the free surface using low (BEM) and high (RANS) fidelity methods

Paolo Perali*[a], Matthieu Sacher[a], Jean-Baptiste Leroux[a], Jeroen Wackers[b], Benoît Augier[c], Frédéric Hauville[d], Patrick Bot[d]

[a] *IRDL, ENSTA Bretagne, CNRS UMR 6027,2 rue François Verny, 29200, Brest, France*
[b] *LHEEA Lab, CNRS UMR 6598, Centrale Nantes, 1 rue de la Noë, B.P. 92101, 44321 Nantes cedex 3, France*
[c] *IFREMER, RDT Research and Technological Development, 1625 Rte de Sainte-Anne, 29280, Plouzané, France*
[d] *IRENav Ecole Navale, BCRM Brest CC600 29240 Brest Cedex 9, France*

Abstract

As a first step toward a multi-fidelity optimization tool for hydrofoils, the present work assesses the ability of the in-house code PUFFIn to be used as a "low-fidelity" solver within the multi-fidelity framework. The code, based on the Boundary Element Method (BEM) and the potential flow theory, is used to study the performance of a typical windsurf hydrofoil operating near the free surface. The hydrofoil is composed of a front wing and a rear stabilizer in a plane-like configuration. Computations are performed for single body configurations (only one wing) and two-body configurations (front wing and stabilizer). First, three linearized models of the free surface are compared for the single front wing configuration with several values of the Froude number: the symmetry, anti-symmetry and Neumann-Kelvin conditions. The results show that for relatively high Froude number, the anti-symmetry and the Neumann-Kelvin conditions provide very similar forces. Then, the predictions of the BEM solver are compared with "high-fidelity" RANS computations, in terms of pressure drag and lift, pressure distribution on the hydrofoil and free surface elevation. Several Froude numbers and submergence depths are studied. The global lift and drag variations predicted by the BEM with the anti-symmetry and Neumann-Kelvin conditions on the single-body configurations are similar to the RANS predictions. For the two-body configurations, the Neumann-Kelvin condition outperforms the anti-symmetry condition. Based on the BEM/RANS comparison, the potential flow solver reveals to be a relevant tool for multi-fidelity optimization.

Keywords: Boundary Element Method, Free surface, Hydrofoils, RANS

*Corresponding author
Email address: paolo.perali@ensta-bretagne.fr (Paolo Perali*)

Nomenclature

β	heel angle
$\boldsymbol{U_0}$	undisturbed flow velocity
$\boldsymbol{u}$	local velocity
Δt	time step
η	free surface elevation
μ	doublet strength
ν	water kinematic viscosity
ϕ	velocity potential
ρ	water density
σ	source strength
σ_{cav}	cavitation number
$\tilde{h}$	normalized depth $\tilde{h} = h/c_{\text{front}}$
c_{front}	chord length of the front wing
c_{stab}	chord length of the stabilizer
C_i	hydrodynamic force coefficient along $i-$axis $(i = x, y, z)$
C_L	lift coefficient
C_p	pressure coefficient $C_p = (p - p_0)/0.5\rho U_0^2$
CM_i	hydrodynamic moment coefficient along $i-$axis $(i = x, y, z)$
Fr_c	Froude number based on the front wing chord $Fr_c = U_0/\sqrt{gc_{\text{front}}}$
g	gravity acceleration
h	submergence depth
p	local pressure
Re	Reynolds number $Re = U_0 c_{\text{front}}/\nu$
S_{front}	planform area of the front wing
s_{front}	span length of the front wing
S_{stab}	planform area of the stabilizer
s_{stab}	span length of the stabilizer
S_B	body surface boundary
S_W	wake surface boundary
S_{FS}	free surface boundary
p_0	undisturbed flow pressure
AGR	Adaptive Grid Refinement
AR	Aspect Ratio
BEM	Boundary Element Method
BIE	Boundary Integral Equation
CFD	Computational Fluid Dynamics
RANS	Reynolds Averaged Navier-Stokes

1. Introduction

Hydrofoils are now widely used in competitive sailing, from boats of the America's Cup to the windsurfers support for the next Olympic games. Such appendices allow lifting a vessel out of the water, thereby reducing the hydrodynamic drag (Molland [31]). The efficiency of a hydrofoil operating close to the free surface strongly depends on the submergence depth and the vessel speed. Thus, numerical predictions of hydrofoils performances have gained interest in the last decades.

Numerical potential methods were historically used due to limited computational resources. Early works on potential flow models about hydrofoils were based on the thin hydrofoil theory (Keldysch and Lawrentjew [23], Hough and Moran [20], Plotkin [39]). To overcome the unrealistic pressure predictions near the leading edge with these approaches, numerical methods for thick hydrofoils were later created by Giesing and Smith [18], based on the 3D Boundary Element Method (BEM) developed by Hess and Smith [19]. To reduce the computational complexity, the non-linear free surface condition can be linearized around the free surface at rest (Bal [2], Yeung and Boucher [51], Nakos and Sclavounos [32]) or the double body solution (Dawson [7], Xie and Vassalos [48]). For steep waves, the non-linearities in the free surface condition has to be considered (Kennell and Plotkin [24], Forbes [15], Longuet-Higgins and Dommermuth [28], Xue et al. [50], Filippas and Belibassakis [13]). With appropriate Green functions, the potential methods were also used to study foils and ships advancing in waves (Xu and Wu [49], Zhang et al. [52]). An unsteady fully non-linear method has recently been proposed by Filippas and Belibassakis [14] to study flapping-wing thrusters in waves. These authors tackled the computational complexity of the fully non-linear method with GPU parallel processing. The boundary element method has also been extended to study cavitating and surface piercing hydrofoils (Bal [3], Bal [4]). However, BEM fails to model wave breaking, due to complex interface reconnections (Lachaume et al. [26]). In addition, potential flow methods do not take into account the viscous effects nor the turbulence and hence they can not provide estimations of the hydrofoil friction drag. On the contrary, RANS (Reynolds Averaged Navier-Stokes) computations can give accurate drag predictions (Esmaeilifar et al. [11]) and model breaking waves (Ni et al. [34]). The experimental work of Duncan [9] has been widely used to validate RANS computations for breaking waves above a hydrofoil (Pernod et al. [38], Di Mascio [8], Karim et al. [21], Prasad et al. [40]). However, despite significant improvements for free surface simulations (Leroyer et al. [27], Wackers et al. [45], Richeux [42]), the computational time of 3D RANS simulations still represents a relatively high computational burden.

Design optimization often have to span a vast variety of design solutions or operating conditions. Thus, the computational resources needed to perform a RANS-based optimization can be a serious impediment to a wide use in the industry (Serani et al. [44]). On the contrary, BEM computations are fast and can be efficiently used in an optimization process (Gaggero et al. [16]). An attractive solution consists in using a multi-fidelity (MF) approach, combining tools with different fidelity levels and computational costs, to

build surrogate models based on a limited number of high-cost simulations (Pellegrini et al. [36], Sacher et al. [43]). In this perspective, a "high-fidelity" RANS solver can be combined to a fast "low-fidelity" BEM to explore a high dimension design space. The objective of the present work is to assess the ability of the in-house BEM code PUFFIn [37] to be used as a "low-fidelity" solver for MF optimization. Multi-fidelity optimization is based on surrogate models of the errors between two fidelity levels. Thus, significant inter-level errors are not a problem, as long as the "low-fidelity" solver does not deteriorate the "high-fidelity" surrogate nor introduce additional uncertainties.

As a MF dedicated tool, PUFFIn is designed to provide fast predictions of the hydrodynamic forces on 3D submerged hydrofoils operating near the free surface. Only steady problems are considered in the present work, leaving the unsteady flows for future investigations. In addition, cavitation effects which might occur for small submergence depths are not studied. For all computations in the present work, the pressure coefficient is higher than the cavitation number ($\sigma_{\text{cav}} = 2.1$ for the highest Froude number investigated). To reduce the computational cost, only linearized free surface conditions are used in this work: a symmetry condition, an anti-symmetry condition and the Neumann-Kelvin condition. The relevance of these linearized models is assessed on a typical windfoil geometry, composed of a front wing and a rear stabilizer. The predictions of the present BEM code are compared with the results of the RANS solver available in the CFD suite FINE/Marine, which can be considered as typical "high-fidelity" computations. To be used as a "low-fidelity" solver, the potential code should be able to capture the global tendencies predicted by the RANS model for the forces variations with the submergence depth and the Froude number values. Two configurations of the hydrofoil are studied. The first configuration (named single-body configuration) consists of a single wing of the hydrofoil, either the front wing or the stabilizer. For the second configuration (named two-body configuration), both the front wing and the stabilizer are considered.

Section 2 presents the theory of the potential flow solver as well as a brief comparison of the PUFFIn predictions with reference 2D test cases available in the literature. The windfoil geometry used for the computations is described in section 3. In section 4, the RANS solver is shortly presented and the numerical setups for the RANS and BEM computations are described. Numerical results obtained with the BEM and RANS methods are given in section 5. A comparative study of the two methods is given, focusing on hydrodynamic forces, pressure distribution and free surface elevation. The results obtained on the single front wing are presented in section 5.1. Results obtained with the potential code for several Froude numbers and the three linearized conditions for the free surface are first presented, to estimate the validity domains of the symmetry and anti-symmetry conditions for the free surface. Then, the influence of the submergence depth is studied for a fixed Froude number, realistic of a windfoil operating condition. For the same Froude number value, numerical results for the two-body configuration are given in section 5.2. The validity of the anti-symmetry condition and Neumann-Kelvin conditions are discussed by comparing the BEM prediction of the forces and moments with the RANS results. Finally, general conclusions and an outlook for future

work are proposed in section 6.

2. Boundary element method

The potential flow solver PUFFIn [37] is presented in this section. After the description of the potential flow equations, the wake generation method and Kutta condition imposed at the trailing edge are presented. Then, the symmetry, anti-symmetry and Neumann-Kelvin conditions are developed from the non-linear free surface condition. This section ends with a brief comparison of the present method with 2D test cases available in the literature.

2.1. General formulation

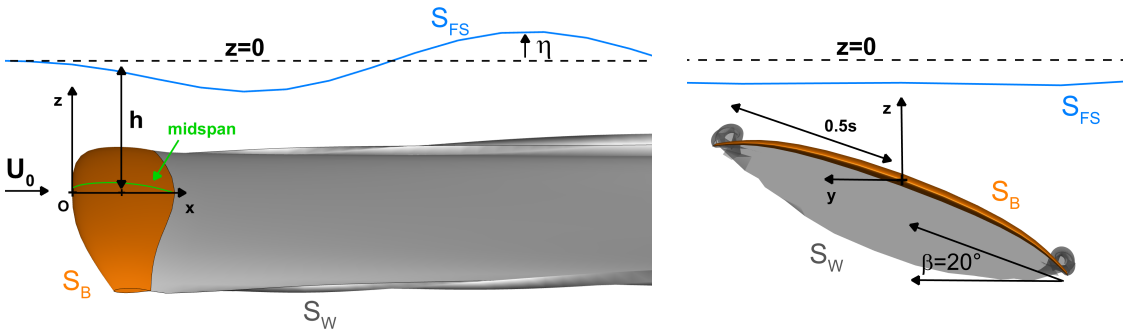

(a) Side view

(b) Front view

Figure 1: Typical configuration of a lifting surface S_B at low immersion h studied with the potential method.

The "low-fidelity" solver is based on an incompressible potential flow approach, i.e. the viscous effects are neglected and the flow is supposed to be irrotational and incompressible. For typical configurations the domain boundary S is the union of the body surface S_B and the free surface boundary S_{FS}. In figure 1, a scheme of such configuration is given for a hydrofoil with a heel angle $\beta = 20°$. The 3D hydrofoil surface is colored in orange and only the 2D free surface elevation at mid-span is drawn in figure 1a for the sake of clarity. The submergence depth h is measured at midchord and midspan of the hydrofoil. According to the Kutta-Joukowsky theorem, a circulation has to exist around the surface S_B to generate a lift force. Since the total circulation in the domain should be null, an additional wake surface S_W should exist to counteract the body circulation (Katz and Plotkin [22]). The Kutta condition imposes the wake surface to start at the trailing edge of the hydrofoil, to ensure finite value of the velocity.

The velocity field $\boldsymbol{u}(\boldsymbol{x},t)$ is obtained as the superposition of the undisturbed flow $\boldsymbol{U}_0$ and the gradient of the perturbation potential $\phi(\boldsymbol{x},t)$:

$$\boldsymbol{u}(\boldsymbol{x},t) = \boldsymbol{U}_0 + \boldsymbol{\nabla}\phi(\boldsymbol{x},t) \tag{1}$$

With these assumptions, the mass conservation reduces to a Laplace equation for the velocity perturbation potential:

$$\boldsymbol{\nabla}^2\phi(\boldsymbol{x},t) = 0 \tag{2}$$

General solutions of the previous equation can be obtained using the Green function of the Laplace equation. For 3D problems, the Green function is given by:

$$\begin{aligned} &\phi_{3\mathrm{D}}(\boldsymbol{x}) = \frac{1}{4\pi r} \\ &\text{with} \quad r = ||\boldsymbol{x} - \boldsymbol{x_P}||,\ P \in S, \end{aligned} \tag{3}$$

Applying the second Green identity to the Laplace equation (Bal [4]), the potential on the boundary S is obtained through a domain Boundary Integral Equation (BIE):

$$\begin{aligned} &\phi(\boldsymbol{x},t) = -\frac{1}{2\pi}\int_S \left[\sigma\frac{1}{r} - \mu\frac{\partial}{\partial n}\left(\frac{1}{r}\right)\right] dS \\ &\text{where} \quad \frac{\partial}{\partial n} = \boldsymbol{n}\cdot\boldsymbol{\nabla}, \text{ with } \boldsymbol{n} \text{ the outward pointing normal vector.} \end{aligned} \tag{4}$$

Equation 4 involves the distributions of doublets μ and sources σ on the boundary S, related with the potential by the relations:

$$\begin{aligned} &\mu(\boldsymbol{x},t) = -\phi(\boldsymbol{x},t) \\ &\sigma(\boldsymbol{x},t) = -\frac{\partial\phi(\boldsymbol{x},t)}{\partial n} \end{aligned} \tag{5}$$

The source strengths on the hydrofoil are given by the non-penetration condition, which states that the flow across the surface S_B is zero (Hess and Smith [19]):

$$\sigma(\boldsymbol{x},t) = -\boldsymbol{U}_0\cdot\boldsymbol{n}, \tag{6}$$

The wake should not support any hydrodynamic loads, i.e., the pressure should be continuous at the hydrofoil trailing edge and across the wake surface. Thus, a non-linear Kutta condition (Kutta [25]) is imposed at the trailing edge to obtain the equality of the pressure on the pressure side and suction side of the hydrofoil:

$$p_{\mathrm{TE}}^{\mathrm{PS}} = p_{\mathrm{TE}}^{\mathrm{SS}} \tag{7}$$

where $p_{\mathrm{TE}}^{\mathrm{PS}}$ is the pressure on the pressure side and $p_{\mathrm{TE}}^{\mathrm{SS}}$ the pressure on the suction side. With the Bernoulli relation, the previous equation might be written:

$$p_{\mathrm{TE}}^{\mathrm{PS}} - p_{\mathrm{TE}}^{\mathrm{SS}} = \left[\rho\frac{\partial\phi}{\partial t} + \frac{1}{2}\rho(\boldsymbol{U}_0 + \nabla\phi)^2 + gz\right]_{\mathrm{PS}}^{\mathrm{SS}} = 0 \tag{8}$$

where $[a]_{\mathrm{PS}}^{\mathrm{SS}}$ is the difference between the pressure side and suction side values of the quantity a. For the steady problem considered in the present work, the time dependency can be removed from the Kutta condition to accelerate the convergence, giving the equation:

$$\left[\frac{1}{2}\rho(\boldsymbol{U}_0 + \nabla\phi)^2 + gz\right]_{\mathrm{PS}}^{\mathrm{SS}} = 0 \tag{9}$$

To ensure that the wake does not support any pressure jump, the sources distribution on S_W must be null and equation 4 can be written (Katz and Plotkin [22]):

$$\phi(\boldsymbol{x},t) = -\frac{1}{2\pi}\int_{S_B+S_{FS}}\left[\sigma(\boldsymbol{x},t)\frac{1}{r} - \mu(\boldsymbol{x},t)\frac{\partial}{\partial n}\left(\frac{1}{r}\right)\right]dS + \frac{1}{2\pi}\int_{S_W}\left[\mu(\boldsymbol{x},t)\frac{\partial}{\partial n}\left(\frac{1}{r}\right)\right]dS \tag{10}$$

In addition, a kinematic condition is imposed on the free surface:

$$\frac{\partial\eta(\boldsymbol{x},t)}{\partial t} + (\boldsymbol{U}_0 + \boldsymbol{\nabla}\phi(\boldsymbol{x},t))\cdot\boldsymbol{\nabla}\eta(\boldsymbol{x},t) = \frac{\partial\phi(\boldsymbol{x},t)}{\partial z} \quad \text{for} \quad z = \eta \tag{11}$$

where $\eta(x,y)$ is the elevation of the free surface. A dynamic condition is also obtained on the free surface with the Bernoulli relation:

$$\frac{\partial\phi(\boldsymbol{x},t)}{\partial t} + \boldsymbol{U}_0\cdot\boldsymbol{\nabla}\phi(\boldsymbol{x},t) + \frac{1}{2}(\boldsymbol{\nabla}\phi(\boldsymbol{x},t))^2 + g\eta = 0 \quad \text{for} \quad z = \eta \tag{12}$$

These two conditions are non-linear since both relations contain quadratic terms and are written on the deformed free surface ($z = \eta$), which is unknown *a priori*. In order to reduce the computation time, linearized conditions are used, as discussed in section 2.2.

2.2. Linearized free surface conditions

In order to fully take into account the non-linearities, the kinematic and dynamic conditions need to be imposed on the deformed free-surface (see Filippas and Belibassakis [14] for a fully nonlinear method). To reduce the computational time, the non-linear free surface conditions can be linearized around the initial free surface position $z = 0$. This latter method is used in the present work. Keeping only the first order terms, the linearized conditions are:

$$\begin{aligned}
&\frac{\partial\eta}{\partial t} + \boldsymbol{U}_0\cdot\boldsymbol{\nabla}\eta = \frac{\partial\phi}{\partial z} \quad \text{in} \quad z = 0\\
&\frac{\partial\phi}{\partial t} + \boldsymbol{U}_0\cdot\boldsymbol{\nabla}\phi = -g\eta \quad \text{in} \quad z = 0
\end{aligned} \tag{13}$$

Combining these two equations, the linear Neumann-Kelvin (NK) formulation is obtained (Brard [6]):

$$\left(\frac{\partial}{\partial t} + \boldsymbol{U_0}\cdot\boldsymbol{\nabla}\right)^2\phi + g\frac{\partial\phi}{\partial z} = 0 \tag{14}$$

Similarly to the Kutta condition, the time derivative can be removed for steady problems and the Neumann-Kelvin condition is:

$$\left(\boldsymbol{U_0}\cdot\boldsymbol{\nabla}\right)^2\phi + g\frac{\partial\phi}{\partial z} = 0 \tag{15}$$

Once the velocity potential is known from equation (15), the free surface elevation η can be obtained from the linear kinematic condition (equation (13)).

The asymptotic analysis of the NK formulation allows to further simplify the free surface condition for very small Froude numbers (Fr<< 1) and very large Froude numbers (Fr>> 1). With a characteristic length of the problem L, a non-dimensional equation might be written for 1-dimensional steady problems (Newman [33]):

$$\frac{\partial^2\phi}{\partial\tilde{x}^2} + \frac{1}{\mathrm{Fr}^2}\frac{\partial\phi}{\partial\tilde{z}} = 0 \quad \text{with} \quad \tilde{x} = \frac{x}{L} \quad \text{and} \quad \tilde{z} = \frac{z}{L} \tag{16}$$

With this formulation, the asymptotic behavior of the NK condition with the Froude number is transparent:

- For Fr$\to$ 0, equation (16) reduces to $\quad \frac{\partial\phi}{\partial\tilde{z}} \approx 0$ at $\tilde{z} = 0$
- For Fr$\to \infty$, equation (16) reduces to $\quad \frac{\partial^2\phi}{\partial\tilde{x}^2} \approx 0 \to \phi = 0$ at $\tilde{z} = 0$

For low Froude numbers, the free surface condition can therefore be replaced by a symmetry condition at $z = 0$, while an anti-symmetry condition (also called biplane approximation) may be used for large Froude numbers (Faltinsen [12]). One advantage of the symmetry and anti-symmetry conditions is that the free surface does not need to be meshed, reducing the computational time and potential numerical errors. Typical Froude numbers for the flow around a hydrofoil are relatively high, such as Fr > 3. Thus, for the highest velocity considered in section 5.1.2 and section 5.2, the predictions obtained with the NK conditions are compared with the anti-symmetry condition. However, the validity domain of this condition in terms of Froude numbers should be investigated, as detailed in section 5.1.1. The symmetry and anti-symmetry conditions are simply obtained by placing a mirrored foil above the free surface with the same or opposite distributions of sources and doublets in the computations.

2.3. Discretisation and resolution

To construct a numerical solution, the boundaries S_B, S_{FS} and S_W are discretized using quadrilateral elements. The sources and doublets are supposed to be constant on each element. This choice to use low-order instead of higher order methods is dictated by the need to reduce the computational time of the low-fidelity solver. The NK condition is solved using the finite difference method, with the second order upwind scheme proposed by Dawson [7] for the spatial derivative:

$$\frac{\partial\phi}{\partial x}(x,t) \approx \frac{120\phi(x,t) - 180\phi(x-\Delta x,t) + 72\phi(x-2\Delta x,t) - 12\phi(x-3\Delta x,t)}{72\Delta x} \tag{17}$$

where Δx is the distance in the streamwise direction between two consecutive panel centers. In Dawson [7] the discretisation of the second order spatial derivatives in equation (15) is obtained by applying this scheme to the velocity computed using a Boundary Integral Equation (BIE). In the present work, the second derivative is obtained by applying twice the scheme given in equation (17) on the potential (see also Bal

and Kinnas [5]). This allows to reduce the computational time since it is more efficient to use the finite difference method than a BIE for the calculation of the velocity. To ensure a proper radiation condition, the first and second spatial derivatives of the potential in the stream-wise direction are imposed to be null at the upstream boundary of the free surface (Nakos and Sclavounos [32]).

The position of the wake surface is an unknown of the problem. The surface S_W could be to prescribe such that the wake leaves the trailing edge at the median trailing angle or that the wake panels are parallel to the undisturbed flow U_0. However, for the two-body configuration, the wake of the front wing can have a strong influence on the incoming flow experienced by the stabilizer. Thus, a more sophisticated wake model is needed. Since the wake should not support any hydrodynamic loads, the Kutta-Joukowski theorem imposes that the wake panels are parallels to the local velocity $\boldsymbol{u}(\boldsymbol{x}, t)$ (Katz and Plotkin [22]). This condition is ensured using a Lagrangian time-marching approach for the construction of the wake surface. At each time step, a new set of panels are shed from the hydrofoil trailing edge and the strength of the doublet μ_w on these panels is obtained with the Kutta condition (equation (8)). The new wake panels are obtained by convecting the trailing edge nodes during one time step, so the size of the wake panels depend on the time step value (figure 2). Once a new panel is shed at the time step n, it is convected by the local flow downstream the hydrofoil at the following time steps $m > n$. According to the Kelvin's circulation theorem, the strength of a wake doublet should not change with time. Thus, once a wake panel is generated at the trailing edge, the value of the doublet μ_w is kept constant while it is convected downstream. Because panels far from the hydrofoil have a small contribution to the flow around the hydrofoil, this time marching method allows to obtain the steady state solution. For some two-body configuration, the wake panels might impinge the stabilizer, leading to numerical instabilities. To avoid such problems, several viscous vortex core models are implemented in PUFFIn following the method proposed by Gennaretti and Bernardini [17]. Details about the viscous core models are not given here, since this kind of wake/stabilizer impingement does not occur with the two-body configuration studied in the present work.

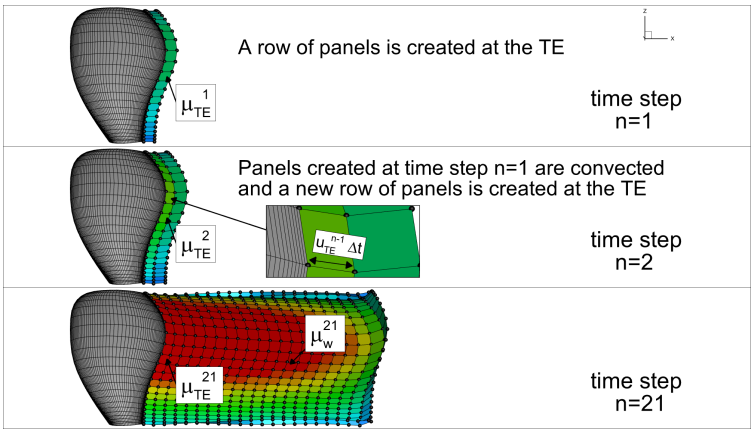

Figure 2: Generation of the wake panels.

While higher order schemes are necessary for true unsteady problems (Filippas and Belibassakis [13]), a first order scheme in time is sufficient to obtain an accurate steady solution with the time-marching algorithm. At time step n, the discretisation of equation (10) at the geometrical center of each element gives:

$$\begin{bmatrix} \boldsymbol{\mathcal{A}_B} & \boldsymbol{\mathcal{A}_{FS}} \end{bmatrix} \begin{bmatrix} \boldsymbol{\mu}_{\boldsymbol{B}}^n \\ \boldsymbol{\mu}_{\boldsymbol{FS}}^n \end{bmatrix} = \begin{bmatrix} \boldsymbol{\mathcal{B}_B} & \boldsymbol{\mathcal{B}_{FS}} \end{bmatrix} \begin{bmatrix} \boldsymbol{\sigma_B} \\ \boldsymbol{\sigma}_{\boldsymbol{FS}}^n \end{bmatrix} + \begin{bmatrix} \boldsymbol{\mathcal{W}}^n & \boldsymbol{\mathcal{T}}^n \end{bmatrix} \begin{bmatrix} \boldsymbol{\mu}_{\boldsymbol{W}}^n \\ \boldsymbol{\mu}_{\boldsymbol{TE}}^n \end{bmatrix} \tag{18}$$

where $\boldsymbol{\mathcal{A}_B}$, $\boldsymbol{\mathcal{A}_{FS}}$, $\boldsymbol{\mathcal{B}_B}$ and $\boldsymbol{\mathcal{B}_{FS}}$ are the matrices containing the influence coefficients for the hydrofoil and the free surface boundaries. The vectors $\boldsymbol{\mu}_{\boldsymbol{B}}^n$, $\boldsymbol{\mu}_{\boldsymbol{FS}}^n$, $\boldsymbol{\sigma}_{\boldsymbol{B}}^n$ and $\boldsymbol{\sigma}_{\boldsymbol{FS}}^n$ contain the values of the doublet and the sources at the time step n on the hydrofoil and free surface panels, respectively. The wake panels are split between the first row of panels at the trailing edge and the rest of the wake panels. Indeed, at each time step, the values of the doublets on the first row of panels $\boldsymbol{\mu}_{\boldsymbol{TE}}^n$ are unknown, whereas the doublets on the rest of the wake panels $\boldsymbol{\mu}_{\boldsymbol{W}}^n$ are known from previous time steps. The matrices $\boldsymbol{\mathcal{T}}^n$ and $\boldsymbol{\mathcal{W}}^n$ contain the influence coefficients of the wake panels. Because the positions of the wake panels change at each time step, these two matrices are therefore time dependent.

In the right-hand side of equation (18), the source strengths on the free surface $\boldsymbol{\sigma}_{\boldsymbol{FS}}^n$ are unknown. These values are obtained using the discretized Neumann-Kelvin equation:

$$\boldsymbol{\mathcal{N}} \boldsymbol{\mu}_{\boldsymbol{FS}}^n = \boldsymbol{\sigma}_{\boldsymbol{FS}}^n \tag{19}$$

where the matrix $\boldsymbol{\mathcal{N}}$ contains the coefficients of the finite difference method (equation (17)).

The unknown values of the doublets on the first row of panels $\boldsymbol{\mu}_{\boldsymbol{TE}}^n$ are obtained from the Kutta condition, which is also discretized using the finite difference method with a second order scheme for the spatial derivative. The discretized Kutta condition can be written:

$$\boldsymbol{\mathcal{M}} \boldsymbol{\mu}_{\boldsymbol{B}}^n = \boldsymbol{\mathcal{K}} \left(\boldsymbol{\mu}_{\boldsymbol{B}}^n \right) \boldsymbol{\mu}_{\boldsymbol{B}}^n \tag{20}$$

with $\boldsymbol{\mathcal{M}}$ and $\boldsymbol{\mathcal{K}}(\boldsymbol{\mu}_{\boldsymbol{B}}^n)$ the matrices containing the coefficients of the finite difference method. Note that, since the Kutta condition is non-linear, the matrix $\boldsymbol{\mathcal{K}}$ depends on the current value of the doublets $\boldsymbol{\mu}_{\boldsymbol{B}}^n$. Combining equations (18), (19) and (20), the unknown doublet distribution on the body and the free surface are obtained by solving:

$$\begin{bmatrix} \mathbf{0} & \tilde{\boldsymbol{\mathcal{M}}} \\ -\boldsymbol{\mathcal{T}}^n & \boldsymbol{\mathcal{A}} \end{bmatrix} \begin{bmatrix} \boldsymbol{\mu}_{\boldsymbol{TE}}^n \\ \boldsymbol{\mu}^n \end{bmatrix} = \begin{bmatrix} \boldsymbol{\mathcal{K}} \left(\boldsymbol{\mu}_{\boldsymbol{B}}^n \right) \boldsymbol{\mu}_{\boldsymbol{B}}^n \\ \boldsymbol{\mathcal{B}_B} \boldsymbol{\sigma_B} + \boldsymbol{\mathcal{W}}^n \boldsymbol{\mu}_{\boldsymbol{W}}^n \end{bmatrix}$$
$$\text{with} \quad \boldsymbol{\mathcal{A}} = \begin{bmatrix} \boldsymbol{\mathcal{A}_B} & \boldsymbol{\mathcal{A}_{FS}} - \boldsymbol{\mathcal{B}_{FS}} \boldsymbol{\mathcal{N}} \end{bmatrix}, \quad \boldsymbol{\mu} = \begin{bmatrix} \boldsymbol{\mu_B} \\ \boldsymbol{\mu_{FS}} \end{bmatrix} \quad \text{and} \quad \tilde{\boldsymbol{\mathcal{M}}} = \begin{bmatrix} \boldsymbol{\mathcal{M}} \\ \mathbf{0} \end{bmatrix} \tag{21}$$

A bloc inversion is used to solve Equation (21). The inverse of the Schur complement $\boldsymbol{\mathcal{C}}^{-1} = \left(\boldsymbol{\mathcal{M}}\boldsymbol{\mathcal{A}}^{-1}\boldsymbol{\mathcal{T}}^{n}\right)^{-1}$ needs to be computed at each time step, since the matrix $\boldsymbol{\mathcal{T}}^{n}$ is time dependant. Nevertheless, the matrix inversion does not require a large computational time because the size of the square matrix $\boldsymbol{\mathcal{C}}$ is only the number of panels on the trailing edge square. The inverse matrix $\boldsymbol{\mathcal{A}}^{-1}$ can be computed only once at the beginning of the simulation with a lower-upper (LU) decomposition. An iterative procedure is used at each time step: the non-linear term $\boldsymbol{\mathcal{K}}\left(\boldsymbol{\mu}_{\boldsymbol{B}}^{n}\right)\boldsymbol{\mu}_{\boldsymbol{B}}^{n}$ is computed using the value of $\boldsymbol{\mu}_{\boldsymbol{B}}^{n}$ at the previous iteration.

Once the velocity potential is known, the pressure distribution on the hydrofoil is obtained with the Bernoulli relation. Integration of the pressure over the surface S_B gives the hydrodynamic pressure forces and moments acting on the hydrofoil.

2.4. Test of the potential method for 2D flows

A succinct validation of the potential method is now presented for the flow around a two-dimensional NACA 4412 near the free surface with $\alpha = 5°$ incidence. Predictions of the present BEM method are compared with 2D numerical results from Yeung and Bouger [51] and Filippas and Belibassakis [13]. Since the present code only handles 3D geometries, a large aspect ratio AR=30 was used for the foil and the lift and drag coefficients were computed at the mid-span section to mimic a 2D flow. The foil surface was discretized using 80 panels along the chord and 11 panels in the span-wise direction. The Neumann-Kelvin condition was used and the dimensions of the free surface were adjusted to get at least three wavelengths downstream the foil and five times the hydrofoil span in the span direction. The free surface was discretized using at least 20 panels per wavelength and 33 panels in the span direction. For all computations, the aspect ratio of the panels on the free surface depends on the wavelength but does not exceed twenty. A typical panel distribution at midspan is given in figure 3d. The time step was set to get $U_0\Delta t/c = 0.5$. Figure 3a shows the lift and drag coefficients predicted by the present BEM for a Froude number based on the chord length $\mathrm{Fr}_c = U_0/\sqrt{gc} = 1$ and several submergence-to-chord ratios h/c. Despite discrepancies on the drag around $h/c = 3$, very good agreement is found between the two methods. For a submergence depth $h/c = 1$, the free surface elevation given by the present BEM for $\mathrm{Fr}_c = 0.7$ and $\mathrm{Fr}_c = 0.9$ is compared with the results obtained by Yeung and Bouger [51] with a 2D hybrid integral equation. The curves are almost identical. The pressure coefficient distribution predicted by the present model for $\mathrm{Fr}_c = 1.03$ and $h/c = 0.6$ is also consistent with the experimental results from Ausman [1] shown in figure 3c.

3. Windfoil geometry

The full geometry of the hydrofoil is composed of a front wing and a stabilizer (figure 4) distant from $d = 0.88$ m, similar to typical configurations used for windsurfer hydrofoils. Both front and rear parts were generated from a H105 profile section. The front wing has a positive camber (camber line above chord

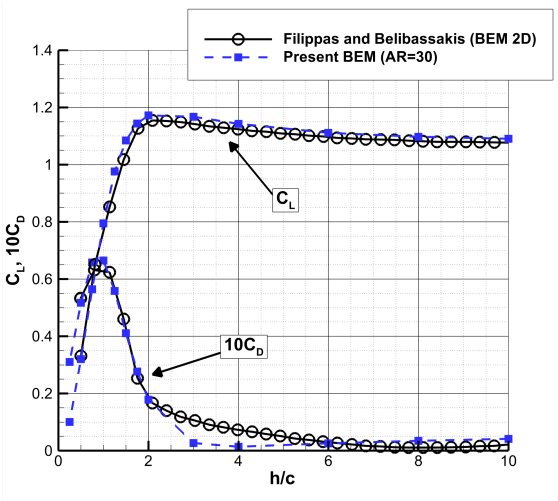

(a) Lift and drag coefficients with varying submergence-to-chord ratio and $\mathrm{Fr}_c = 1.0$

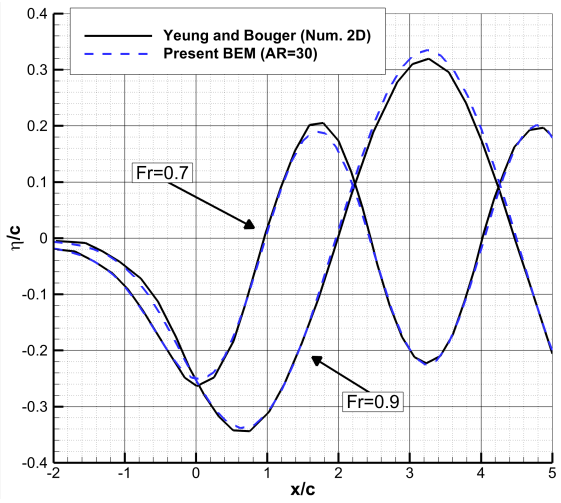

(b) Free surface elevation predicted for two values of the Froude number and $h/c = 1$. The leading edge is located at $x/c = -1$.

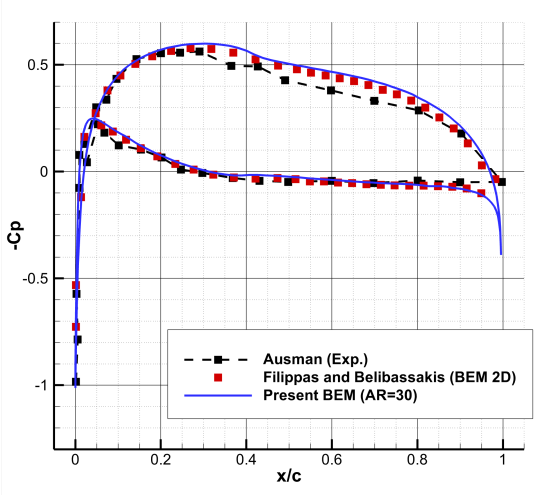

(c) Pressure coefficient obtained on the foil with $\mathrm{Fr}_c = 1.03$ and $h/c = 0.6$

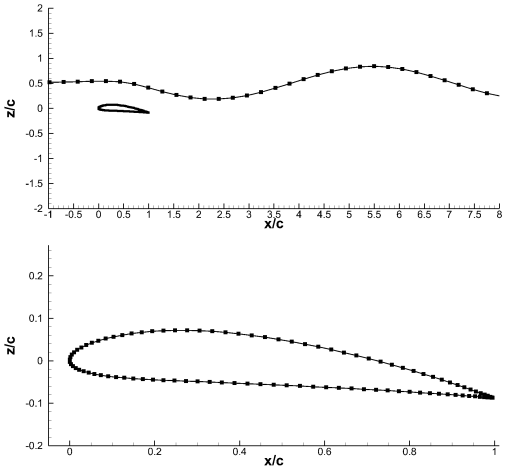

(d) Panels distribution at midspan on the hydrofoil and the free surface for $\mathrm{Fr}_c = 1.0$ and $h/c = 0.5$.

Figure 3: Comparison of the present BEM predictions for the flow around a NACA 4412 hydrofoil with 2D numerical results from Filippas and Belibassakis [13] and Yeung and Bouger [51] and experimental measurement from Ausman [1]. The angle of attack is $\alpha = 5°$ and the aspect ratio is AR=30 for the present BEM results.

line) while the stabilizer has a negative camber (camber line below chord line). Thus, the lift force created by the front wing is directed upwards and the lift force of the stabilizer is directed downwards. Both the front wing and the stabilizer are located at the same height. The dimensions and angles of the two wings are given in table 1. The maximum chord lengths are located at mid-span and are $c_{\mathrm{front}} = 0.12$ m for the front wing and $c_{\mathrm{stab}} = 0.08$ m for the stabilizer. The front wing and stabilizer span are $s_{\mathrm{front}} = 0.5$ m and $s_{\mathrm{stab}} = 0.25$ m, respectively. Full geometry (CAD) is available upon request to the contact author.

Computations performed using only one of the two wings are referred to as "single-body configuration". Most of the single-body computations have been performed with the single front wing (see section 5.1), but a few computations are also presented with the single stabilizer in section 5.2.1. Computations with the full hydrofoil, i.e. with both the front wing and the stabilizer, are referred to as "two-body configuration" (see section 5.2). The foil is located at a distance h under the free surface at rest (plane $z = 0$) with a heel angle $\beta = 20°$. Computations were performed for several immersion depths h and flow velocities U_0. The immersion depth h is defined as the distance between the interface at rest and the front wing leading edge at mid-span. The front wing chord length at mid-span c_{front} is used as the reference length to reduce to a dimensionless equation. The submergence-to-chord ratio is defined as $\tilde{h} = h/c_{\text{front}}$ for both the single-body and two-body configurations. The Froude number is computed as $\text{Fr}_c = U_0/\sqrt{gc_{\text{front}}}$.

Table 1: Dimensions and angles of the front wing and the stabilizer.

Parameter	Front wing	Stabilizer
Section	H105	H105
Chord at mid-span	0.12 m	0.08 m
Span	0.5 m	0.25 m
Anhedral/Dihedral angle	8.19°	8.19°
Sweep angle (LE root to LE tip)	11.69° (backward)	11.69° (forward)
Twist angle	-2°	-2°
Rake angle	2°	2°

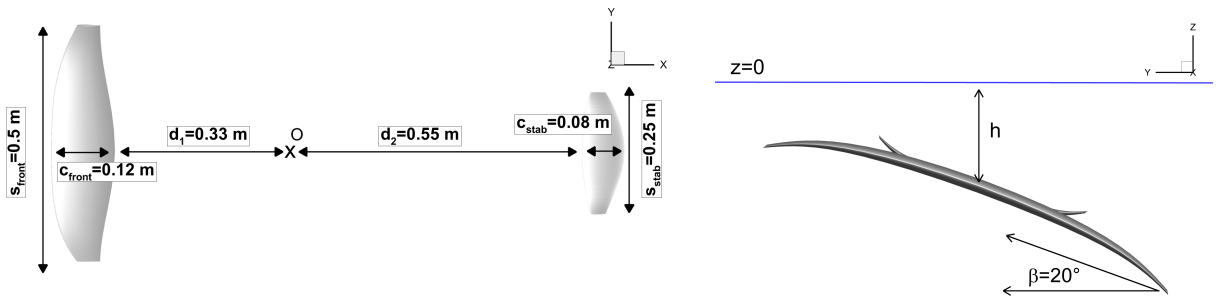

(a) Top view

(b) Front view

Figure 4: Description of the hydrofoil geometry.

4. Simulation setup

The setups of the BEM and RANS computations are presented in this section. Preliminary computations were first performed with PUFFIn to select an appropriate mesh providing fast and accurate results. Then,

the RANS solver is briefly presented.

4.1. BEM computations

A grid convergence study was first performed with the front part of the wing in an infinite domain. The inflow velocity was set to $U_0 = 9.76$ m/s ($\mathrm{Fr}_c = 9$) and three grids were generated (G3, G2 and G1 from the coarsest to the finest). Finer panels were used near the leading edge, the trailing edge and the tips of the wings, as illustrated in figure 5a. As shown in table 2, the relative differences obtained for the lift and drag coefficients with the grids G1 and G2 are less than 0.5%. The medium grid G2 was therefore considered fine enough to produce grid-independent solutions and was used for computations with the free surface.

Table 2: Grid convergence study around the front wing in infinite domain ($U_0 = 9.76$ m/s).

Grid	Panels along the chord	Panels along the span	ΔC_x	ΔC_L
G3	80	12	4.0%	-1.1%
G2	112	24	0.5%	-0.1%
G1	160	48	-	-

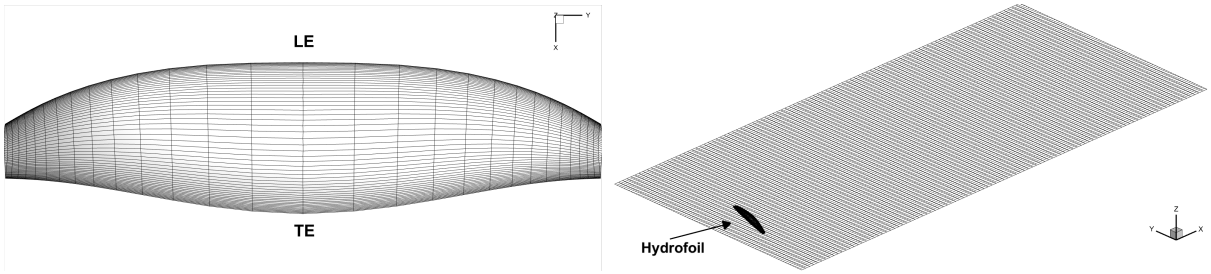

(a) Top view of the grid G2 used for the front wing.

(b) The free surface is discretized using 100 panels along the x-direction and 80 panels along the y-direction.

Figure 5: Hydrofoil and free surface meshes used for Fr_c=9.

The free surface was discretized with a Cartesian grid to get at least 20 panels per wavelength and at least 10 panels per wingspan in the span-wise direction. Preliminary tests on the front wing performed for $\mathrm{Fr}_c = 0.6$ and $\mathrm{Fr}_c = 9$ with $\tilde{h} = 0.83$ showed that increasing the number of panels in the stream-wise and span-wise directions by a factor 1.5 led to less than 0.4% differences on the hydrodynamic coefficients. The discretisation using 20 panels was thus considered fine enough to get reliable predictions without prohibitively increasing the computation time. The dimensions of the free surface mesh were adjusted with the Froude number to ensure at least three wavelengths downstream the hydrofoil and five chord lengths upstream. For large Froude numbers such as $\mathrm{Fr}_c = 9$, the wavelength is very long and it is not necessary to capture three wavelengths in the wake of the hydrofoil to correctly compute the hydrodynamic forces. Again, preliminary

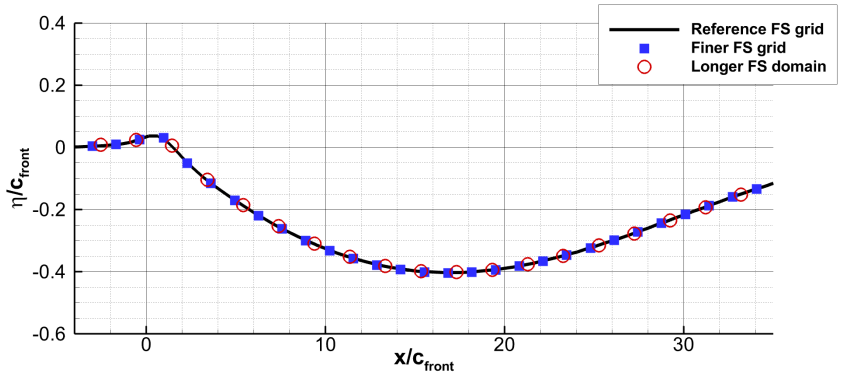

Figure 6: Influence of the free surface discretisation and free surface dimensions on the wave elevation at mid-span ($\mathrm{Fr}_c = 9$, $\tilde{h} = 0.83$).

tests done by increasing the free surface dimensions by 50% did not show significant variations of the hydrodynamic coefficients or the free surface elevation for $\mathrm{Fr}_c = 0.6$ and $\mathrm{Fr}_c = 9$ with $\tilde{h} = 0.83$ (see figure 6). An example of the free surface mesh is given in figure 5b for $\mathrm{Fr}_c = 9.0$. For computations with the two-body configuration, i.e front wing and stabilizer, the stabilizer was discretized using the same number of panels as presented for the grid G2 in table 2. For the flow conditions investigated in the present work, steady solutions are expected and the time step value was not found to have a significant impact on the results. Thus the time step was set to get $\Delta t U_0 / c_{\mathrm{front}} = 0.5$. The computations are stopped when the variations of the forces are less than 0.5% of the value averaged over the last 70 time steps. For most of the cases investigated, convergence is reached within 150 time steps. The roll-up of the vortex wake obtained at convergence for Fr_c=9 and $\tilde{h} = 0.83$ is visible in figure 7.

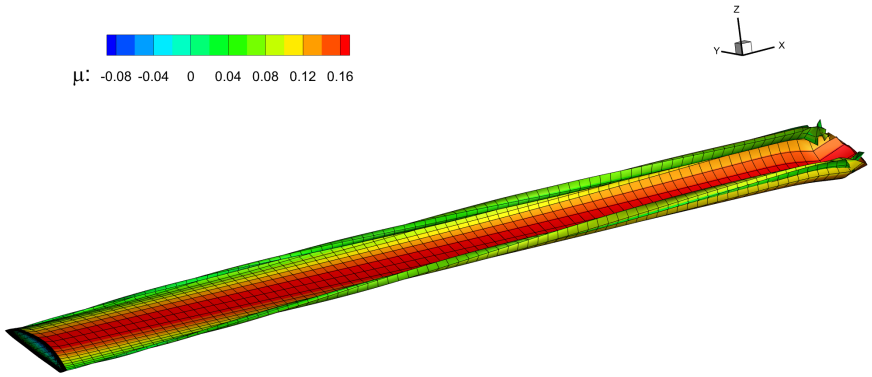

Figure 7: Wake surface obtained at the end of the computation for the front wing with Fr_c=9 and $\tilde{h} = 0.83$. The forces have converged within 84 time steps.

4.2. Viscous flow computations

The viscous flow results taken as high-fidelity references are obtained with the CFD suite FINE/Marine, commercialized by CADENCE. The flow solver ISIS-CFD included in FINE/Marine is developed by Ecole Centrale de Nantes (Nantes, France) and is based on a finite volume method to solve the URANS (Unsteady Reynolds Averaged Navier-Stokes) equations. The influence of the turbulence is taken into account with the $k-\omega$ SST model (Menter [29]). For the Reynolds numbers considered in this work the boundary layer is not fully turbulent and the standard $k-\omega$ SST model can not accurately capture the boundary layer. More accurate models such as the $\gamma-\mathrm{Re}_\theta$ transition model (Menter and Langtry [30]) or Large Eddy Simulation should be used to properly capture the turbulent transition of the boundary layer. However, within a typical optimization framework it is not possible to use such models which need finer meshes and hydrofoil optimization are generally performed using standard RANS models. In addition, preliminaries computations with the $\gamma-\mathrm{Re}_\theta$ model suggested that large flow separation of the laminar boundary layer is not expected for the test case investigated, and that the turbulent transition mainly results in an offset of the total drag force. Consequently, the optima obtained by an optimization procedure with the standard $k-\omega$ SST model are expected to be close to the ones obtained with a transition model. The boundary layer transition also strongly depends on the turbulence intensity of the flow, which is difficult to estimate in situ for computations. Finally, for most applications with competitive sailing yachts the Reynolds number based on the foil chord is greater than Re$= 10^6$, so that the boundary layer is almost fully turbulent. This is why, the effect of the boundary layer transition is neglected in the present work and the standard $k-\omega$ SST model is used.

A mixture-model approach is used to capture the free surface (Queutey and Visonneau [41]). The convective fluxes are discretized using the AVLSMART scheme, which is a blending between a third order QUICK scheme and an upwind first order scheme. The mass fraction equation is discretized with the BRICS scheme (Wackers et al. [47]). Unstructured hexahedral meshes are generated with the software HEXPRESS, included in the FINE/Marine suite. Simulations are performed using Adaptive Grid Refinement (AGR, see Wackers et al. [46]), to reduce the computational time and accurately capture the free-surface and physics of the flow around the hydrofoil. A second-order backward Euler scheme is used for the temporal discretisation.

The computational domain extends from $32c_{\mathrm{front}}$ upstream the front wing leading edge to $42c_{\mathrm{front}}$ downstream the stabilizer trailing edge, sideways from $-48c_{\mathrm{front}}$ to $48c_{\mathrm{front}}$ and vertically from -$40c_{\mathrm{front}}$ below the free surface to $24c_{\mathrm{front}}$ above the free surface. The velocity and volume fraction are imposed on the inlet and the side planes. The pressure is imposed on the top and bottom planes. The wall function is used on the hydrofoil surface.

The RANS computations were setup following the procedure described by Richeux [42] to perform accurate simulations with AGR. For the sake of brevity, only the main parameters of the AGR procedure are presented. First an initial coarse mesh was generated with HEXPRESS to use a wall function in the

hydrofoil boundary layer ($y^+ \approx 60$). The AGR procedure is then called repeatedly during the computation to refine the initial mesh. A combined criterion based on the grid size for cells normal to the free surface and a flux components Hessian threshold is employed (Wackers et al. [46]). For all computations, the target size for cells normal to the interface is set at $c_{\text{stab}}/64 \times 1.2$. The Hessian threshold is set to $c_{\text{stab}}/16$ and the minimum cell size is set to $c_{\text{stab}}/256 \times 1.2$. Horizontal refinement was limited to a box around the hydrofoil, ending $6.4c_{\text{front}}$ downstream the hydrofoil. The AGR procedure is called every 20 time steps during the computations. As discussed in Richeux [42] and Pernod et al. [38], those parameters allow getting small numerical uncertainties on the solution for surface piercing and submerged hydrofoil with a significant reduction of the computational time compared to computations without AGR. A grid convergence study for the two-body configuration is given in Appendix A. An example of initial coarse mesh and adaptively refined mesh is presented in figure 8. As expected, the final mesh is refined in the area of interest, i.e. around the hydrofoil, close to the free surface and in the wakes. With the present setup, typical initial grids for the single front wing contain around 0.5 M cells (1.2 M cells for the case of the two-body configuration) and the final refined meshes contain about 15 M cells (21 M cells for the case of the two-body configuration). Following the guidelines proposed by Richeux [42], the time step was set to $\Delta t = 0.05c_{\text{stab}}/U_0$.

5. Results and discussion

The results obtained with the BEM and RANS methods are first presented in section 5.1 for the single front wing configuration. Then, the comparison of the two numerical approaches for the two-body configuration is given in section 5.2.

5.1. Single-body configuration: front wing

In this section, numerical predictions of the potential and the viscous flow approaches are compared for the flow around the single front hydrofoil. The influence of the Froude number on the hydrodynamic forces and free surface patterns is investigated in section 5.1.1. In section 5.1.2, several submergence depths are considered for one high Froude number of interest, $\text{Fr}_c = 9$.

5.1.1. Influence of the Froude number

Potential flow computations were performed with the Neumann-Kelvin (NK), symmetry and anti-symmetry free surface conditions, to study the asymptotic behavior of the NK model with the Froude number. The submergence depth was kept constant at $h = 0.1$ m ($\tilde{h} = 0.83$) and the inflow velocity was changed to get Froude numbers between $\text{Fr}_c = 0.4$ and $\text{Fr}_c = 9$. Since the BEM does not capture the viscous part of the forces, only the pressure contributions of the forces $F_{i,P}$ are taken into account to compute the hydrodynamic coefficients for both the potential and viscous flow computations:

$$C_i = \frac{F_{i,P}}{0.5\rho U_0^2 S_{\text{front}}} \quad \text{for} \quad i = x, y, z \tag{22}$$

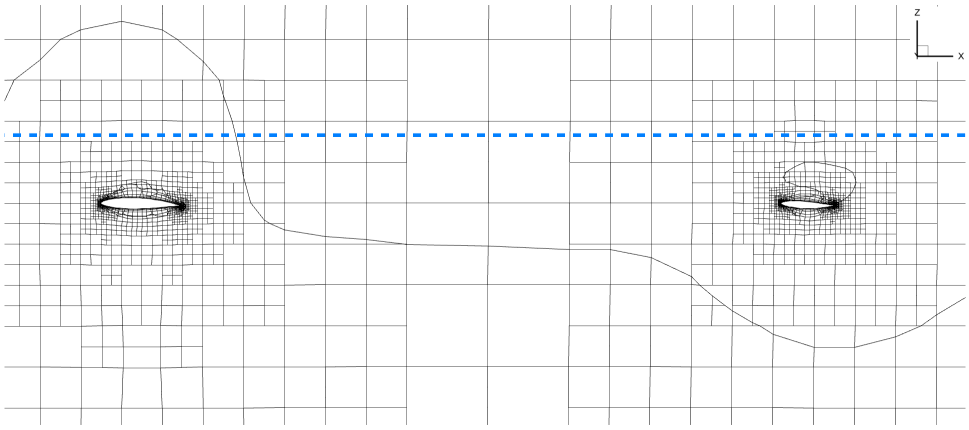

(a) Initial mesh

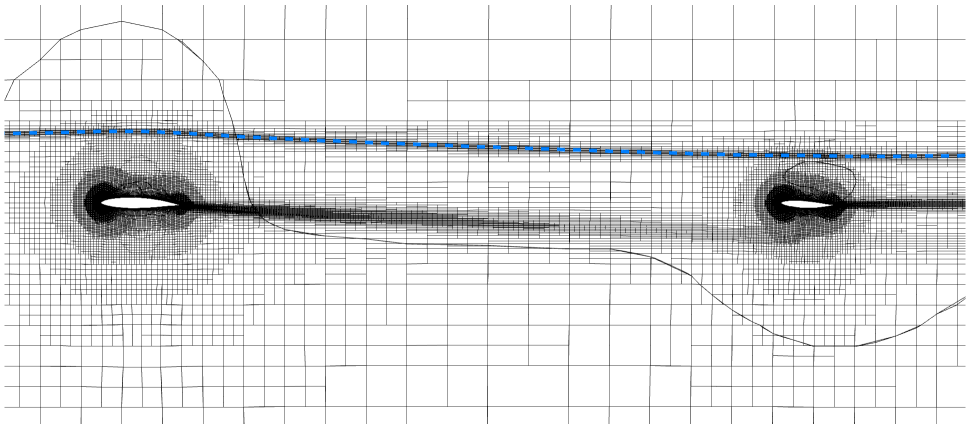

(b) Final mesh with AGR

Figure 8: Example of adaptive grid refinement used in the RANS computations. The blue dashed line depicts the interface.

where S_{front} is the planform area of the front wing.

The hydrodynamic force coefficients of the foil obtained with the three free surface conditions are presented in figure 9. The coefficients predicted by the symmetry and anti-symmetry conditions remain constant for the Froude numbers investigated. For C_y and C_z, the absolute values are higher with the symmetry condition. As presented in figure 11, these differences are due to a smaller pressure coefficient on the suction side for the symmetry condition. Indeed, this condition acts as a wall above the foil, increasing the forces perpendicular to the oncoming flow direction F_y and F_z. Note that the force in the y-direction is negative, due to the heel angle of the hydrofoil. With the symmetry condition the minimum pressure is located on the port side of the flow, while it is on the starboard side with the anti-symmetry condition. The drag coefficient C_x is slightly higher with the anti-symmetry condition than the one predicted with the symmetry condition. The differences on the drag between the two conditions are much smaller than the differences observed for the vertical and side forces. This is because the drag force is mainly due to the location of

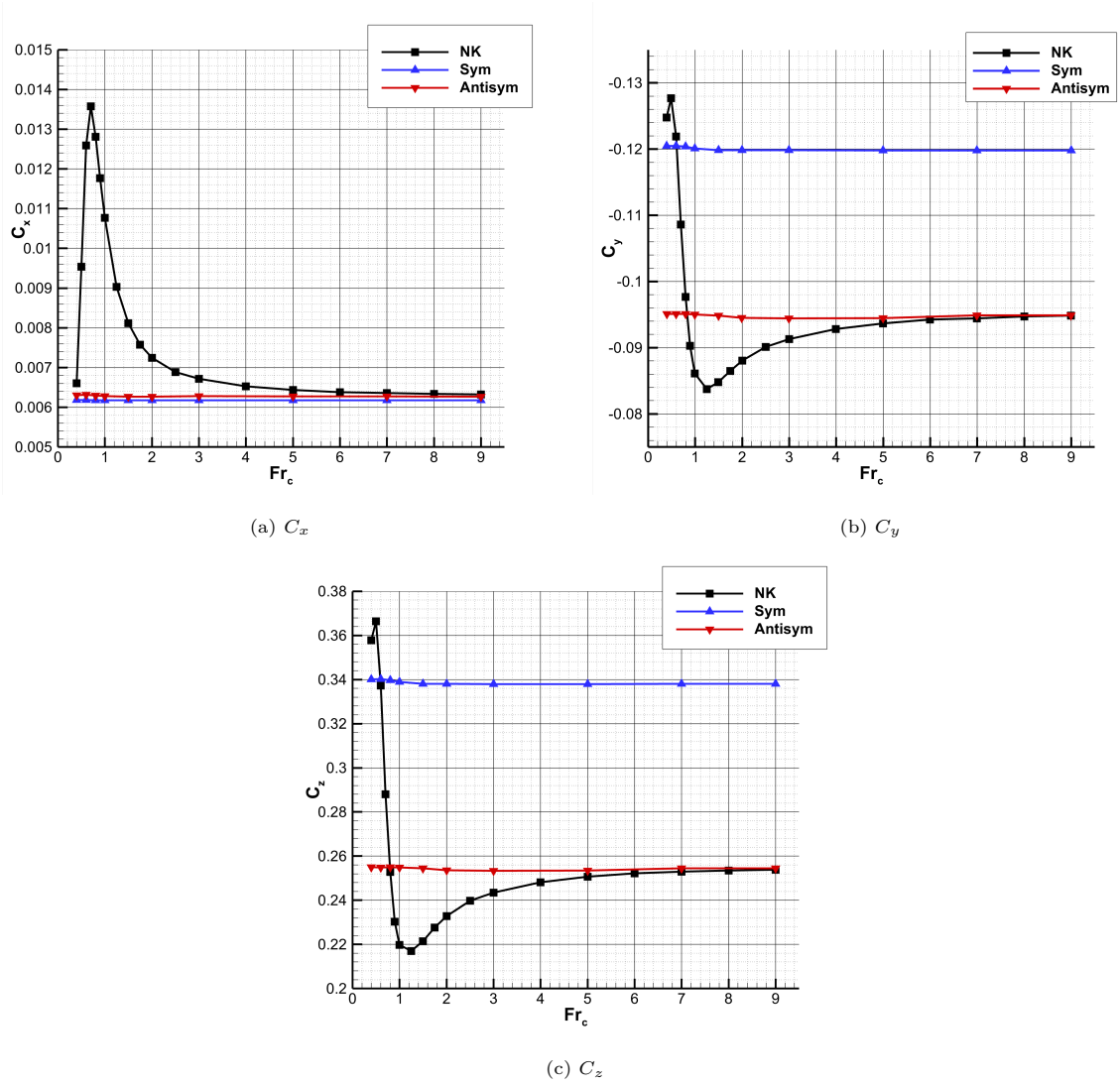

(a) C_x

(b) C_y

(c) C_z

Figure 9: Comparison of the hydrodynamic force coefficients predicted by the Neumann-Kelvin (NK), symmetry (Sym) and anti-symmetry (Antisym) free surface conditions for several Froude numbers Fr_c. The submergence depth is $\tilde{h} = 0.83$.

the stagnation point on the pressure side of the foil and the pressure distribution on the pressure side does not change significantly between the two conditions (figure 11). As expected, the coefficients predicted by the Neumann-Kelvin condition are close to the ones obtained with the anti-symmetry condition for high Fr_c and closer to the ones given by the symmetry conditions for low Fr_c. For intermediate values of the Froude number, the NK predictions move away from the asymptotic curves, with local extrema around $\mathrm{Fr}_c = 0.5$ and $\mathrm{Fr}_c = 1.25$ for C_y and C_z and one extremum at $\mathrm{Fr}_c = 0.5$ for C_x. Similar variations of the moment coefficients are observed in figure 10. The coefficient CM_x is positive for the symmetry condition and negative for the anti-symmetry condition. This is due to the location of the minimum pressure, which

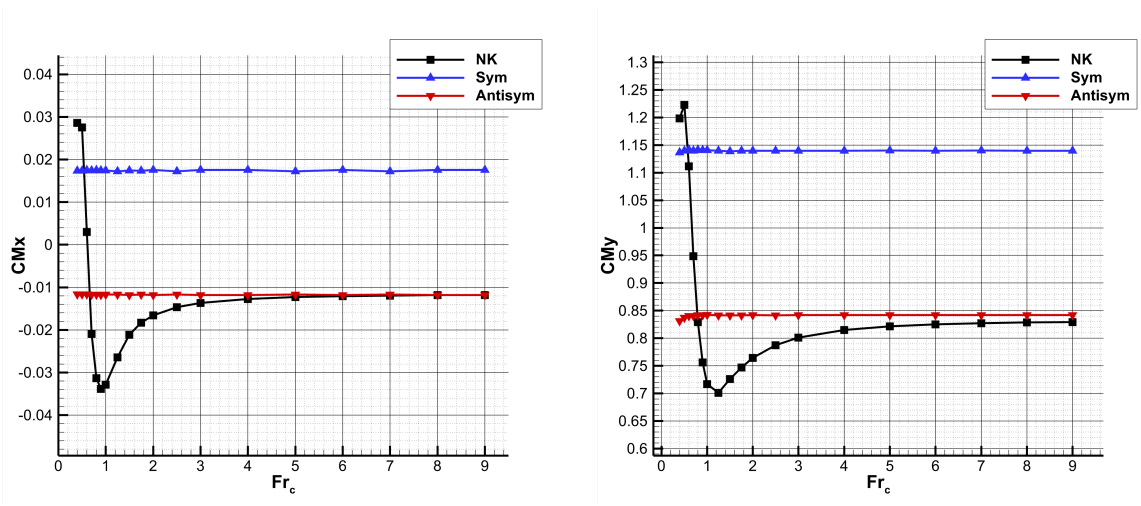

(a) CM_x (b) CM_y

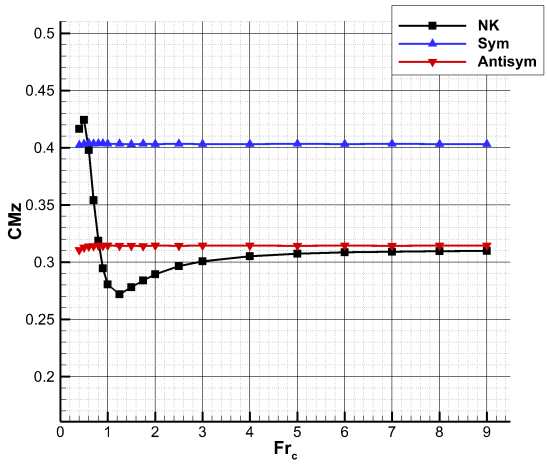

(c) CM_z

Figure 10: Comparison of the hydrodynamic moment coefficients predicted by the Neumann-Kelvin (NK), symmetry (Sym) and anti-symmetry (Antisym) free surface conditions for several Froude numbers Fr_c. The submergence depth is $\tilde{h} = 0.83$.

moves from the port side to the starboard side of the foil when the Froude number increases (figure 11). The present results suggest that the symmetry condition might be used instead of the NK condition for $\mathrm{Fr}_c \leq 0.6$, while the anti-symmetry condition is valid for $\mathrm{Fr}_c \geq 5.0$ for the single front wing configuration at the investigated submergence depths.

For moderate Reynolds numbers, laminar to turbulent transition of the boundary layer is expected. Moreover, flow separation may occur on the suction side of the foil. The present potential flow approach can not model either of these phenomena. Thus, in the following, only Froude numbers larger than one are considered for the comparison between the low and high-fidelity methods. Moreover, foiling configurations

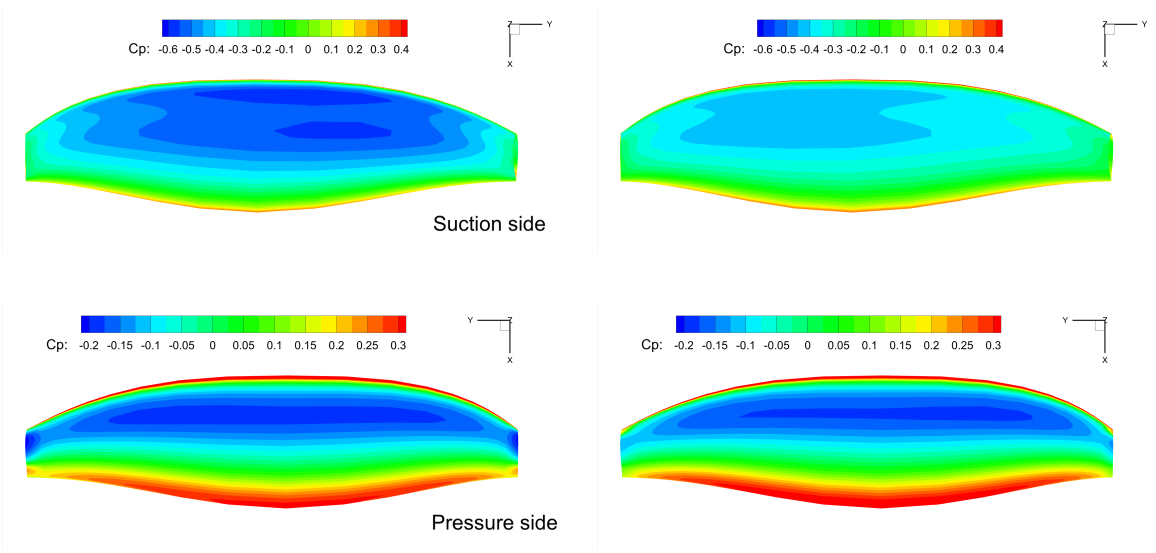

(a) Symmetry condition

(b) Anti-symmetry condition

Figure 11: Distribution of the pressure coefficient for the symmetry and anti-symmetry conditions ($\mathrm{Fr}_c = 9$, $\tilde{h} = 0.83$)

are not expected for Froude numbers larger than 1, corresponding to Reynolds numbers greater than Re$= 1.3 \times 10^5$, for which the influence of the laminar to turbulent transition is smaller on the hydrodynamic forces.

In figure 12, the hydrodynamic coefficients predicted by the BEM code with the NK condition are compared to RANS results for the same range of Froude number and three submergence-to-chord ratios ($\tilde{h} = 0.83; 1.00; 1.50$). A significant offset is visible between the RANS and BEM C_y and C_z curves. The potential method gives a 30% overestimation of the hydrodynamic lift forces compared to the viscous approach. This over-prediction may be expected since the development of the boundary layer in the RANS computation tends to decrease the effective camber of the hydrofoil, thus reducing the contribution of the lift forces to the oncoming flow. Indeed, additional computations with ISIS-CFD without viscosity and turbulence model have shown excellent agreement with the BEM computations (see Appendix B). This strongly suggests that the discrepancies between RANS and BEM results are due to the boundary layer. Nevertheless, the global shapes of the curves obtained with the potential flow approach are in good agreement with the viscous flow results. Particularly, for the Froude numbers considered, the free surface condition is similar to an anti-symmetry condition and the lift forces decrease when the foil gets closer to the interface. For the three submergence depths considered, the potential and viscous flow computations predict a local extremum for C_y and C_z. These extrema occur at different Froude numbers, depending on the submergence depth.

As presented in figure 13, the variations in the hydrodynamic coefficients are linked to significant changes in the free surface elevation caused by the hydrofoil. For high Froude number ($\mathrm{Fr}_c = 6.0$), a large trough appears relatively far from the hydrofoil, around $x/c_{\mathrm{front}} \approx 10$. The BEM method is able to predict the

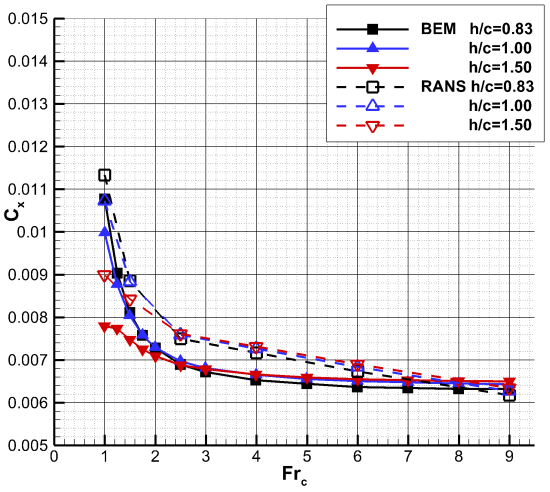

(a) C_x (pressure drag)

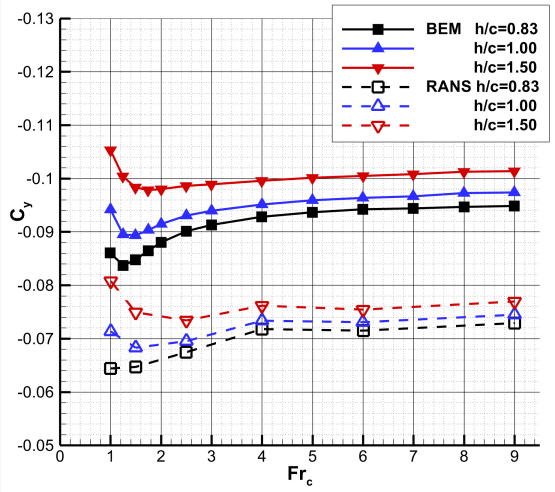

(b) C_y

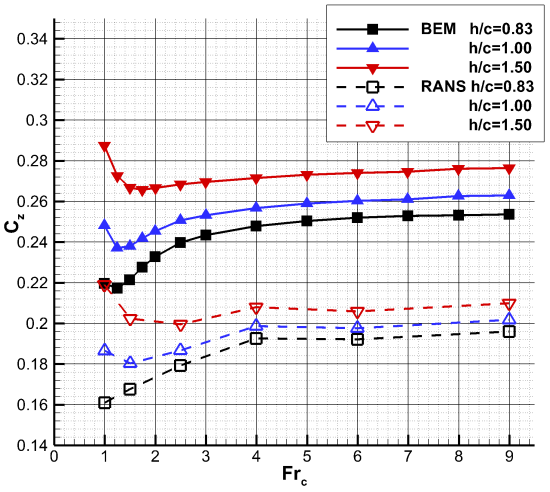

(c) C_z

Figure 12: Comparison of the hydrodynamic coefficients predicted by the potential code (NK conditions) with the ones predicted by RANS computations for several Froude numbers Fr_c. Three submergence depths are considered $\tilde{h} = 0.83$, $\tilde{h} = 1.00$ and $\tilde{h} = 1.50$. Only the contributions due to the pressure are used to compute the forces coefficients for both methods.

trough location, but slightly overestimates the waves amplitude, particularly for $x/c_{\text{front}} \geq 20$. This is mainly due to the viscous diffusion of the wake in the RANS computation, whereas the doublet strengths in the wake are kept constant with the potential flow method. When the Froude number decreases to $\text{Fr}_c = 1.0$, the trough is closer to the hydrofoil. The waves amplitude also tends to decrease when the Froude number decreases. Unlike the BEM results, the wave elevation in the RANS computation decreases downstream the hydrofoil. This damping was also observed with preliminary computations using finer grids at the interface. Thus, the damping of the wave profile is rather due to viscous effects than numerical diffusion. For $\text{Fr}_c = 6.0$ and $\text{Fr}_c = 1.0$, the maximum free surface deformations are obtained on the port side (negative y values), corresponding to the deepest part of the foil, where the minimum pressure occurs on the suction side (figure 14). For $\text{Fr}_c = 1.0$, the pressure coefficient decreases on the pressure side, leading to a smaller value of the lift coefficient compared to the one obtained at $\text{Fr}_c = 6.0$.

The potential flow method is able to predict consistent free surface deformations and pressure distribution with the RANS results for several values of the Froude number. Particularly, the BEM code provides a good estimation of the forces variations with the Froude number, with an offset compared to the RANS results. A full coupling between the potential tool and a boundary layer code might permit to correct this offset. Nevertheless, this offset is not a problem to build a surrogate model with the BEM code for an optimization process. Indeed, if the variations of the forces are accurately captured, the extrema locations of the surrogate model remain the same and the "low-fidelity" tool can be efficiently used for multi-fidelity optimization.

5.1.2. Influence of the submergence depth ($Fr_c = 9$)

The influence of the submergence depth on the front foil hydrodynamic coefficients was further investigated for $\text{Fr}_c = 9$. Potential and viscous flow computations were performed for depth ratios between $\tilde{h} = 6.0$ and $\tilde{h} = 0.50$. For the BEM, the Neumann-Kelvin and anti-symmetry conditions were also compared for this high Froude number. The variations of the drag coefficient C_x and the lift coefficient $C_L = \sqrt{C_y^2 + C_z^2}$ are given in figure 15. The variation of θ, defined as the angle between the lift force and the vertical, is also presented. The predictions of the pressure drag coefficient C_x obtained with the anti-symmetry condition are very similar to the ones given by the Neumann-Kelvin condition with the BEM method. Except the existence of an offset, overall good agreement is found between the potential and viscous flow coefficients. Both methods predict a non-monotonic variation of the drag coefficient, with a maximum value around $\tilde{h} = 1.50$. For smaller submergence depth, the drag drastically decreases. For the smallest submergence depth, the anti-symmetry condition seems to overestimate the drag reduction. The potential method overestimates the lift compared to the RANS model. This overestimation exists for the highest submergence-to-chord ratio, where the influence of the free surface is small. Thus, these discrepancies may be due to the lack of a boundary layer model in the BEM rather than the free surface model, as explained in section 5.1.1. Nevertheless, the lift monotonically decreases with the submergence-to-chord ratio. For $\tilde{h} > 2.0$, the vari-

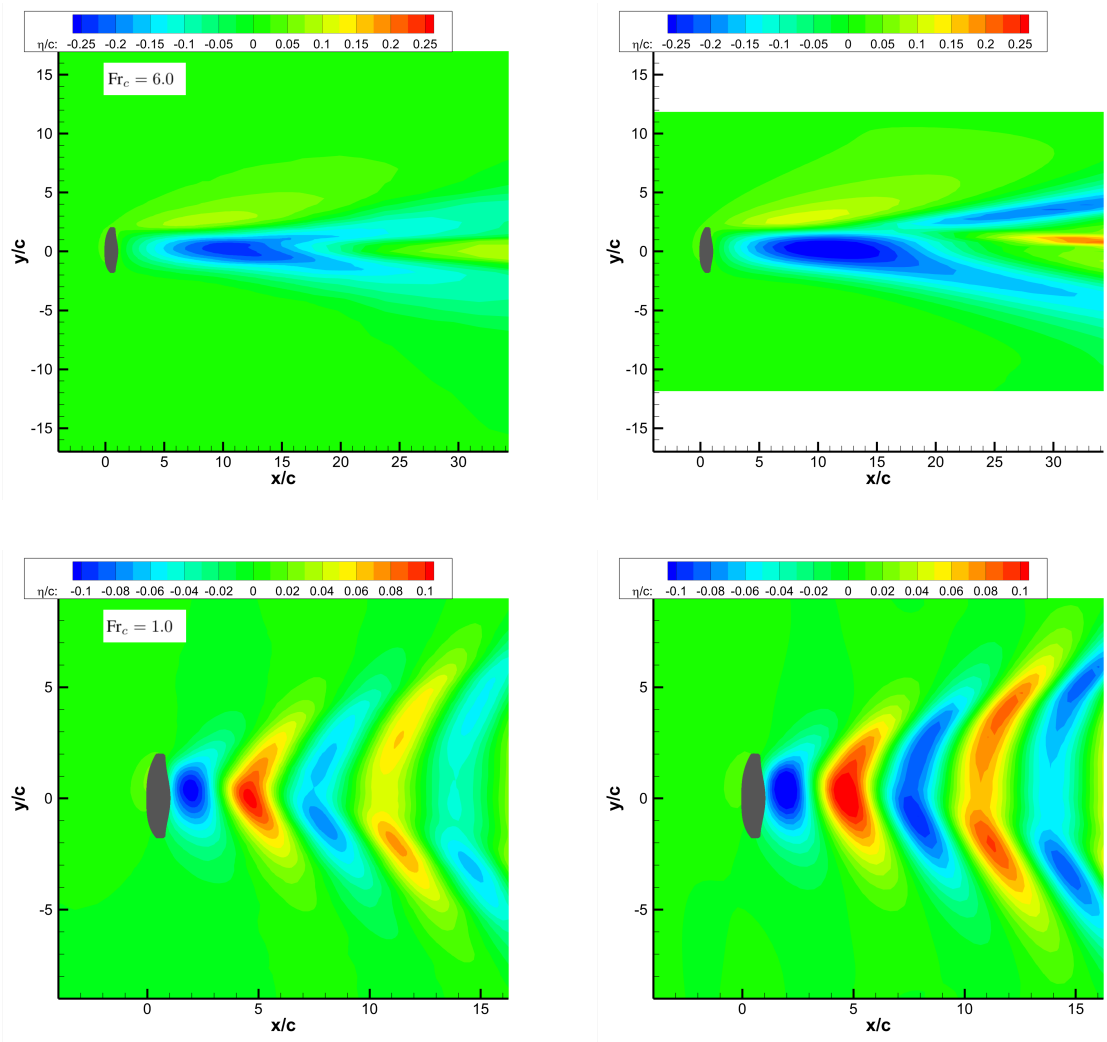

Figure 13: Free surface elevation predicted by RANS computations (left) and BEM computations with the Neumann-Kelvin condition (right) for $\mathrm{Fr}_c = 6.0$, $\mathrm{Fr}_c = 1.0$ and $\mathrm{Fr}_c = 0.5$. The submergence depth is $\tilde{h} = 0.83$.

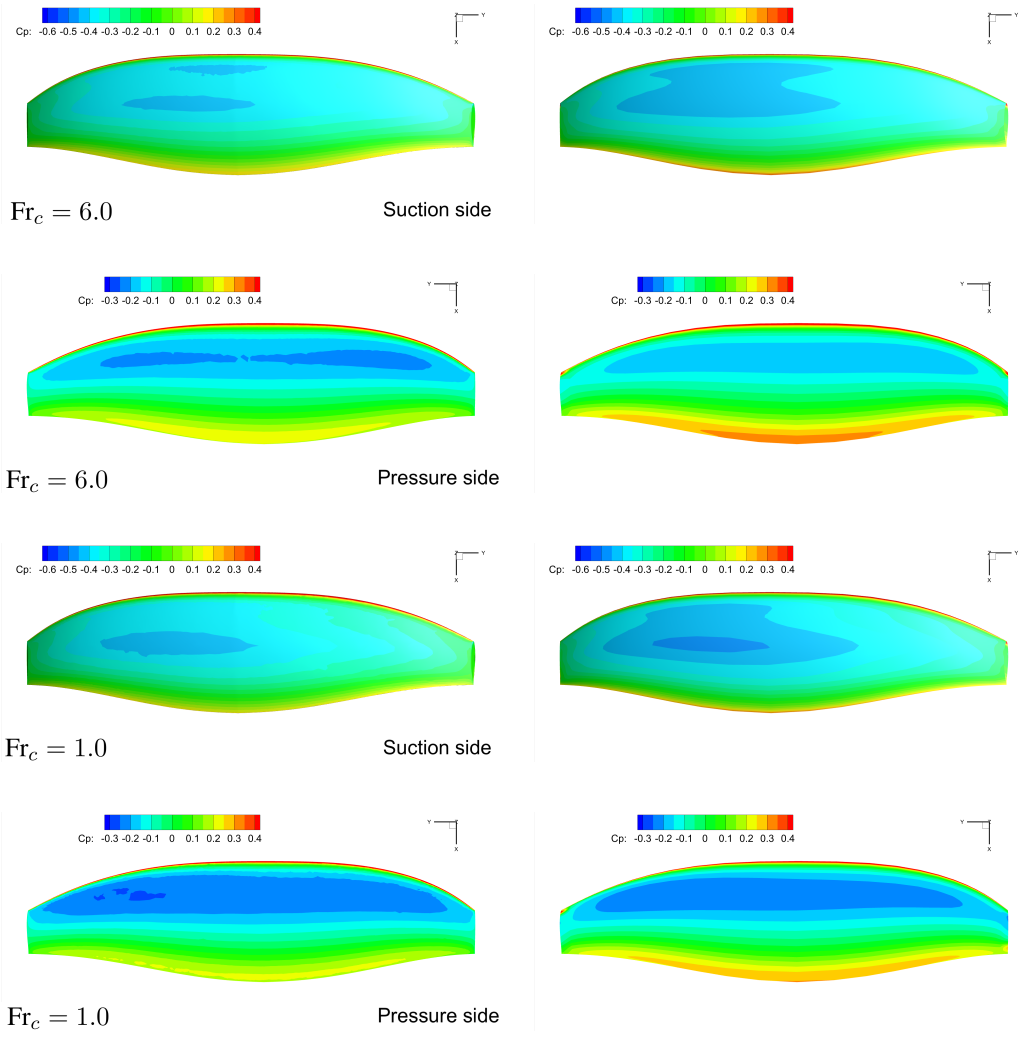

Figure 14: Comparison of the pressure distribution on the front wing obtained with the RANS (left) and BEM (right) computations for different Froude numbers ($\tilde{h} = 0.83$).

ations of the hydrodynamic coefficients are smaller than 2%. For smaller values of $\tilde{h}$, the relatively strong decrease of the lift is observed. The relative reduction of the lift between the largest and the smallest ratio $\tilde{h}$ is $\Delta C_L = -21\%$ in the RANS computations and $\Delta C_L = -28\%$ for the potential predictions. Thus, while the BEM is not able to predict accurate values of the lift, the variation of the force is well captured by the potential flow approach. The value of θ is equal to the heel angle for the deepest submergence and slightly increases when the foil gets closer to the interface (about 1° for RANS and 2° for potential computations).

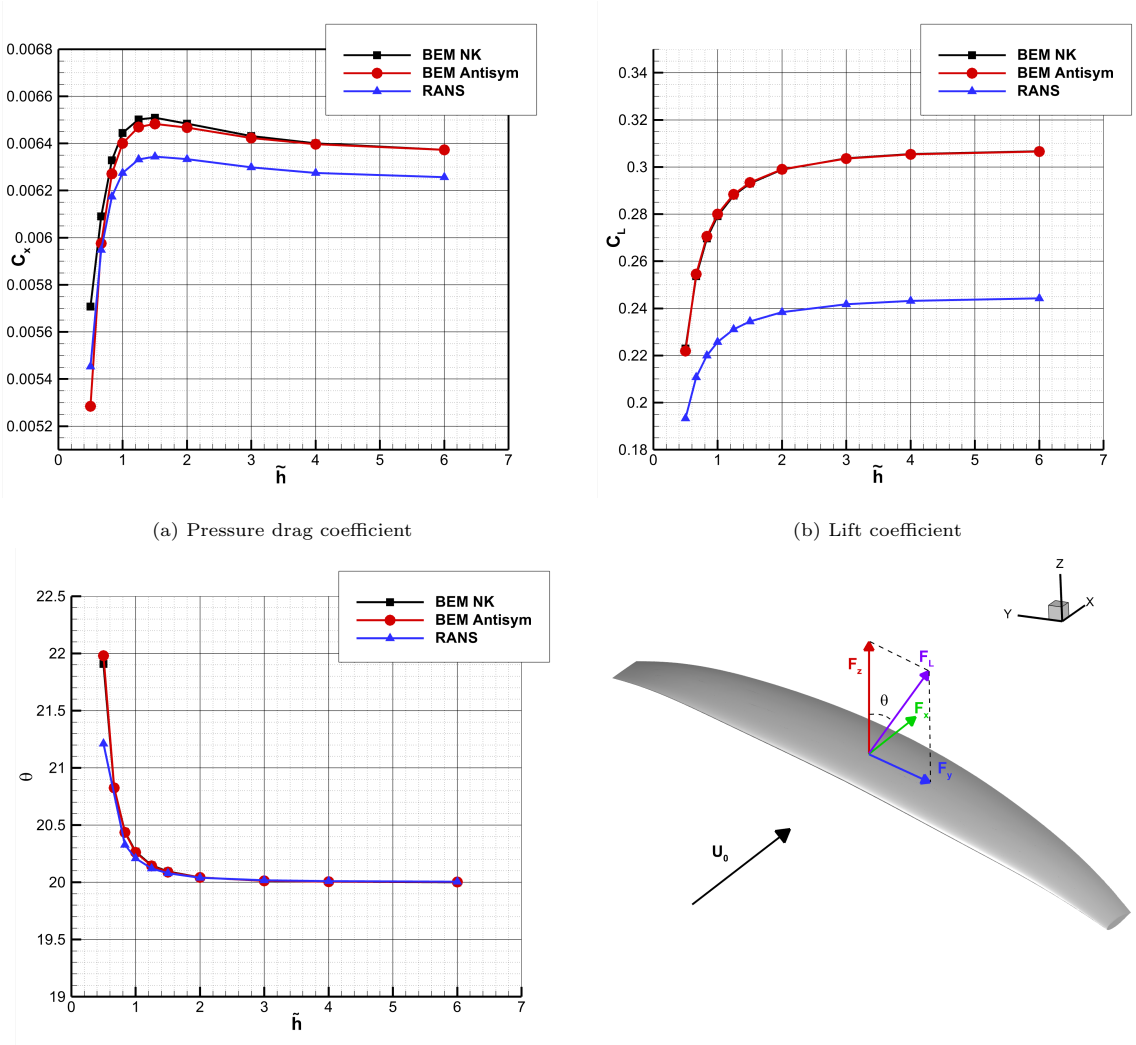

(a) Pressure drag coefficient

(b) Lift coefficient

(c) Angle θ

Figure 15: Comparison of the hydrodynamic coefficients obtained with the BEM and RANS computations for the single front wing at $\mathrm{Fr}_c = 9$ and varying submergence-to-chord ratio ($\tilde{h} = h/c_{\mathrm{front}}$).

The pressure coefficient distributions on the suction side obtained for four submergence-to-chord ratios between $\tilde{h} = 6.00$ and $\tilde{h} = 0.50$ are presented in figure 16 for the RANS and BEM computations with

the NK condition. As expected, the pressure distribution is symmetric with respect to the mid-span plane for the deepest immersion. The minimum pressure is weaker in the BEM simulations due to the lack a of boundary layer model, but the region of low pressure is in good agreement with the RANS results. Both methods predict an increase of the pressure on the suction side when the foil gets closer to the free surface. For small submergence depths ($\tilde{h} \leq 0.83$) the pressure distribution is no longer symmetric and the minimum pressure is obtained on the deepest part of the hydrofoil (port side, $y < 0$), producing an increase in the angle θ. Because of the heel angle, the free surface tends to reduce the load on the shallowest part of the hydrofoil (starboard side), while the deepest part is less affected. The pressure coefficients obtained with the anti-symmetry condition are very similar to the ones given by the Neumann-Kelvin condition and thus not presented for the sake of conciseness.

5.2. Two-body configuration: front wing and stabilizer ($Fr_c = 9$)

In this section, results are presented for the two-body configuration (front wing and stabilizer) to assess the ability of the potential flow method to provide reliable estimations of the forces variations for high Froude numbers. The Froude number was set to $\mathrm{Fr}_c = 9$ and the submergence depth was changed between $\tilde{h} = 6$ and $\tilde{h} = 0.5$. To better understand the reciprocal influence of the two wings, a few computational results are also presented for the single-body configuration with the stabilizer only. In this, section a distinction is made between the hydrodynamic coefficients computed on the front wing, the stabilizer and the full geometry (front wing and stabilizer). The hydrodynamic coefficients for the stabilizer and the full hydrofoil are computed in a similar manner than equation 22:

$$
\begin{aligned}
C_i^{\mathrm{front}} &= \frac{F_{i,P}^{\mathrm{front}}}{0.5\rho U_0^2 S_{\mathrm{front}}} \quad \text{for the front wing,} \quad i = x, y, z \\
C_i^{\mathrm{stab}} &= \frac{F_{i,P}^{\mathrm{stab}}}{0.5\rho U_0^2 S_{\mathrm{stab}}} \quad \text{for the stabilizer,} \quad i = x, y, z \\
C_i^{\mathrm{tot}} &= \frac{F_{i,P}^{\mathrm{front}} + F_{i,P}^{\mathrm{stab}}}{0.5\rho U_0^2 (S_{\mathrm{front}} + S_{\mathrm{stab}})} \quad \text{for the full hydrofoil,} \quad i = x, y, z
\end{aligned}
\tag{23}
$$

where S_{front} and S_{stab} are the planform areas of the front wing and stabilizer, respectively. The lift coefficient is still defined by $C_L = \sqrt{C_y^2 + C_z^2}$ for all cases.

5.2.1. Analysis of the front wing/stabilizer interaction

Computations with the two-body configuration are compared with the ones performed on the single front wing to estimate the influence of the stabilizer on the interface. Figure 17 shows the free surface elevation obtained for $\mathrm{Fr}_c = 9$ and $\tilde{h} = 0.83$ for the two configurations with the RANS computations and BEM (with the NK condition). As discussed in section 5.1.1 the BEM gives stronger variations of the free surface. With both methods, the high pressure on the upper part of the stabilizer induces a smaller trough in the wake.

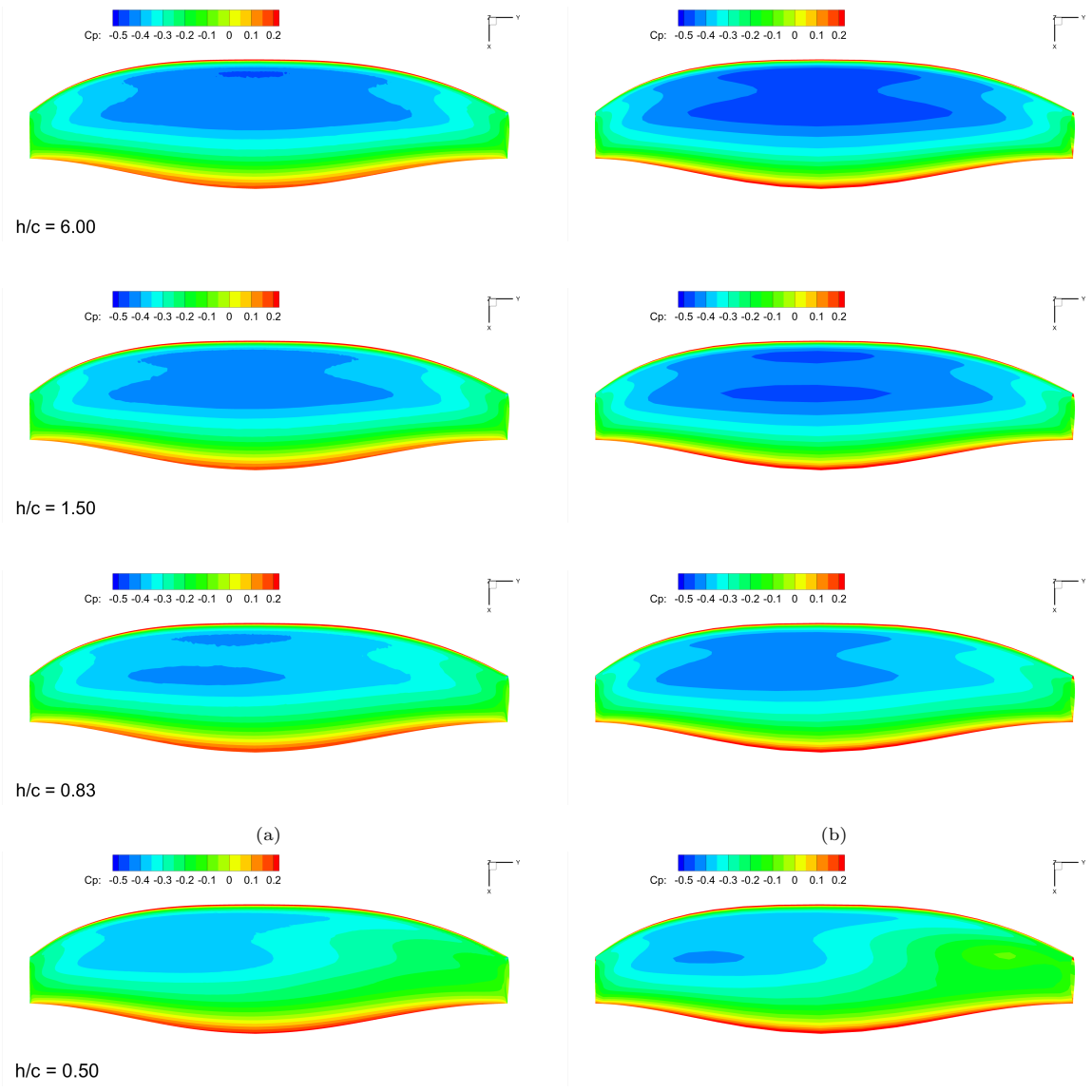

Figure 16: Pressure distribution on the suction side for the single front wing configuration at $\mathrm{Fr}_c = 9$ and varying submergence-to-chord ratio.

The computations also show a shift of the minimum free surface elevation to the starboard side which is due to the asymmetric distribution of the pressure on the stabilizer.

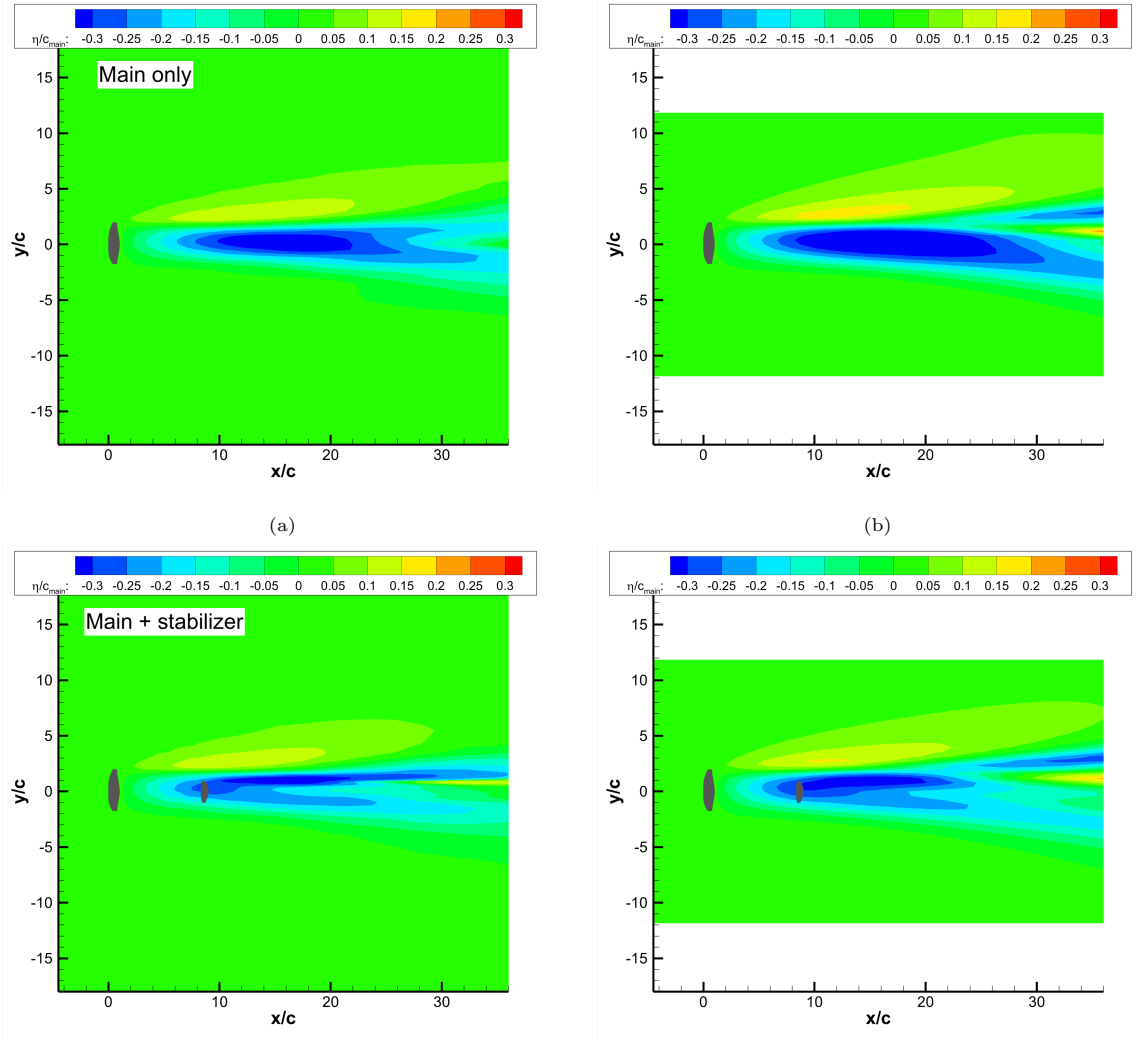

(a) (b)

(c) RANS (d) BEM

Figure 17: Comparison of the free surface elevation predicted by the RANS (left) and BEM (right) computations for the single front wing (top) and the two-body configuration (bottom). $\mathrm{Fr}_c = 9.$ and $\tilde{h} = 0.83$.

The front wing coefficients C_x^{front} and C_L^{front} obtained with the two-body configuration are presented in figure 18. The coefficients obtained on the single front wing configuration (section 5.1) are also plotted for comparison (gray dashed lines). While the lift coefficient is not affected by the stabilizer with both approaches, the drag coefficient of the front wing is slightly smaller in the RANS computations for $\tilde{h} > 0.83$. However, these differences are less than 1% and can be due to numerical errors. On the contrary, the coefficients predicted by the NK and the anti-symmetry condition are similar and very close to the ones

obtained for the single front wing configuration.

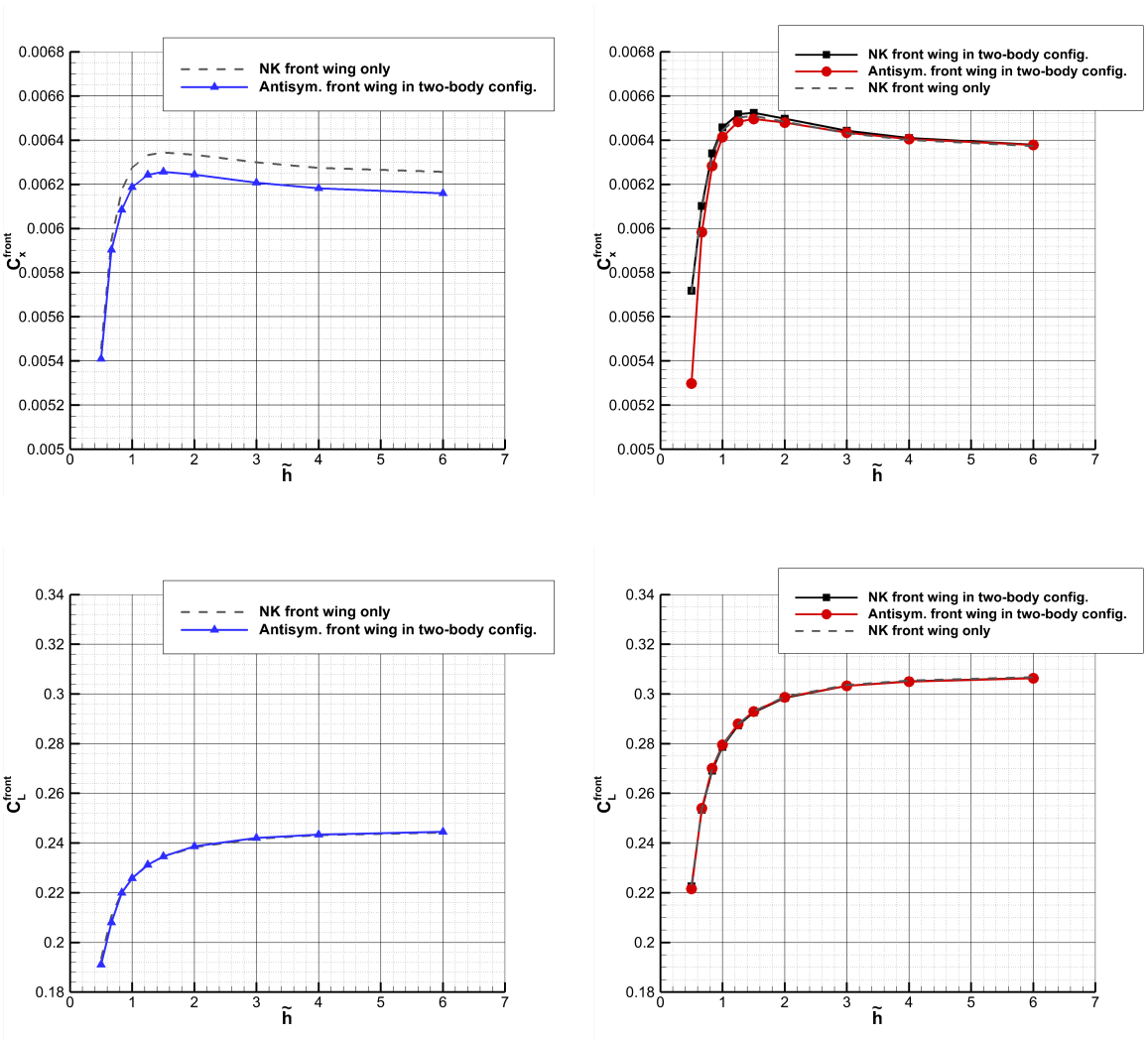

(a) RANS (b) BEM

Figure 18: Hydrodynamic coefficients obtained on the front wing in the two-body configurations with the RANS (left) and BEM (right) computations ($\mathrm{Fr}_c = 9$). Only the pressure contribution of the forces is used to compute the coefficients. The grey dashed lines depict the coefficients obtained on the single front wing configuration.

The stabilizer coefficients C_x^{stab} and C_L^{stab} obtained with the two-body configuration are presented in figure 19. Additional computations were performed for the single stabilizer configuration to assess the influence of the front wing on the stabilizer forces. The hydrodynamic coefficients obtained for the single-body configuration are plotted as gray dashed lines in figure 19. With the definition of the lift coefficient (23), the coefficient C_L^{stab} is always positive, but one should keep in mind that the lift created by the stabilizer is directed downwards. While an offset still exists between the RANS and BEM results, both methods predict negative values of the drag when the stabilizer is located in the front wing wake. Because the front wing

induces a deviation of the flow, the apparent inflow for the stabilizer is no longer aligned with the x-axis. Consequently, the downwash from the main wing results in a propulsive contribution of the stabilizer's lift. The pressure drag increases in the RANS and BEM results when the submergence depth decreases. On the contrary, the lift produced by the stabilizer is greater in presence of the front wing. In fact, the flow deviation induced by the front wing also tends to increase the effective incidence of the stabilizer. Moreover, while the lift of the single stabilizer tends to slightly increase with smaller ratio $\tilde{h}$, the lift significantly decreases when the stabilizer is downstream the front wing.

The variations of the drag and lift forces with the submergence depth are much larger in the two-body configuration. Indeed, $h/c_{\text{stab}} = 1.5h/c_{\text{main}}$, so the influence of the free surface is expected to be smaller for the single stabilizer than for the main wing. In addition, the suction side of the stabilizer is the lower side of the foil, where the influence of the free surface is smaller compared to the upper side. The larger force variations with the submergence depth observed for the two-body configuration suggest that the forces on the stabilizer strongly depend on the wake of the front wing: the proximity of the free surface modifies the pressure distribution on the front wing, which in turn has a strong influence on the apparent inflow seen by the stabilizer.

Figure 19 also highlights differences between the coefficients provided by the NK and anti-symmetry conditions. Particularly, the anti-symmetry condition gives a significant increase of the lift coefficient around $\tilde{h} = 0.83$, in discrepancy with the RANS predictions. Indeed, the pressure distribution on the stabilizer is affected by the trough located in the wake of the front wing and the differences observed between the NK and the anti-symmetry conditions suggests that this influence might not be accurately captured by the latter.

5.2.2. Variations of the total forces and moments acting on the full hydrofoil

The variations of the coefficients C_x^{tot} and C_L^{tot} for the full hydrofoil predicted by the BEM and RANS computations are given in figure 20. Regarding the drag, larger differences between the potential and the viscous flow approaches are obtained compared to the single front wing configuration. With the NK condition the drag is higher than the reference value ($\tilde{h} = 6$) for all the smaller submergence depths. In the contrary, the RANS computations show that the drag obtained for $\tilde{h} = 0.5$ is smaller than the one obtained for $\tilde{h} = 6$. However, both methods predict a maximum value of the drag around $\tilde{h} = 1$. Besides, the anti-symmetry condition gives a significantly smaller value than the RANS prediction for $\tilde{h} = 0.5$. This is due to the poor prediction of the drag on the stabilizer by the anti-symmetry condition (figure 19). Thus the NK condition might outperform the anti-symmetry condition for the drag estimation. The variations of the lift coefficient obtained with the two free surface conditions are similar. Compared to the RANS results, the BEM overestimates the lift reduction when the full hydrofoil gets closer to the free surface.

The moments acting on the hydrofoil are also of interest since they might jeopardize the stability of the watercraft. The dimensionless moment coefficients for the full geometry are given by:

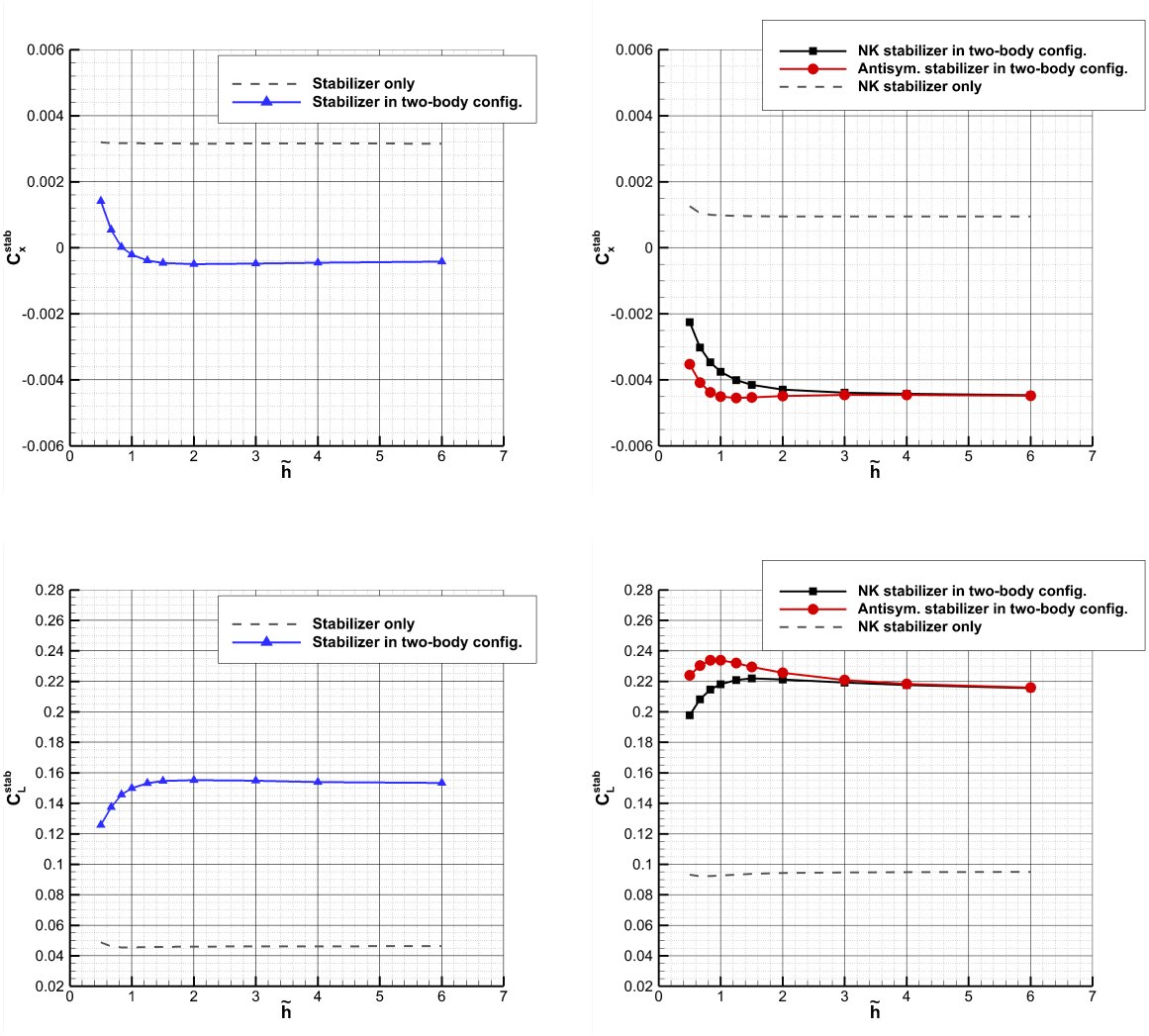

(a) RANS (b) BEM

Figure 19: Hydrodynamic coefficients obtained on the stabilizer in the two-body configuration with the RANS (left) and BEM (right) computations ($\mathrm{Fr}_c = 9$). Only the pressure contribution of the forces is used to compute the coefficients. The grey dashed lines depict the coefficients obtained on the single stabilizer configuration.

$$CM_i = \frac{M_{i,P}^{\text{front}} + M_{i,P}^{\text{stab}}}{0.5\rho U_0^2 (S_{\text{front}} + S_{\text{stab}})(c_{\text{front}} + c_{\text{stab}})} \quad \text{for} \quad i = x, y, z \tag{24}$$

where the pressure moments $M_{i,P}$ are computed about the point O in figure 4, which would roughly be the location of the junction between the fuselage and the hydrofoil mast in a real configuration. The moment coefficients are presented in figure 21. As the hydrofoil gets closer to the free surface, a negative rolling moment appears, which is overestimated by the potential flow approach. This moment is very small compared to the other moments and tends to reduce the windward heel. In fact, it represents a shift of the

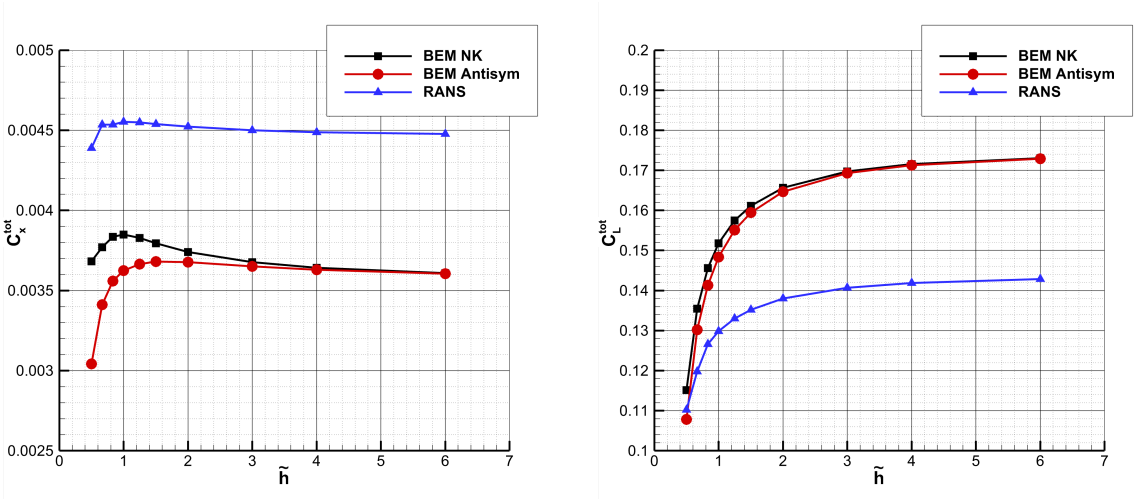

(a) C_x (b) C_L

Figure 20: Total pressure hydrodynamic coefficient predicted by the RANS and BEM computations for the two-body configuration ($\mathrm{Fr}_c = 9$).

force application point smaller than 4 cm toward port side. With both the BEM and RANS computations, the yaw and pitch moments decrease when the submergence depth decreases. These reductions of the moments are strongly linked to the reductions of the lift force when the foil becomes closer to the free surface. As for the forces, an offset exists between the potential and viscous results. However, the BEM code is able to capture the variations of the moments: with both BEM and RANS approaches, the moments M_y and M_z at $\tilde{h} = 0.83$ are about 20% smaller than the moments at $\tilde{h} = 6$.

6. Conclusion

The present work assessed the ability of the BEM code PUFFIn to be used as a "low-fidelity" within a multi-fidelity optimization process. The BEM solver was designed to predict the performances of 3D hydrofoils operating near the free surface with a relatively small computational time. Numerical predictions of the potential solver were compared with "high-fidelity" RANS computations for the flow around a submerged hydrofoil composed of a front wing and a stabilizer. Three linearized free surface conditions were compared for the BEM: the symmetry, anti-symmetry and Neumann-Kelvin conditions. The RANS computations were done with adaptive grid refinement, using a combined criterion based on the free surface and the flux component Hessian. Computations were performed on single-body configurations and two-body configurations, analyzing the pressure drag and lift, as well as free surface waves patterns.

For the single front wing configuration, the influence of the Froude number was first investigated. Potential flow results suggest that the Neumann-Kelvin condition is similar to a symmetry condition for $\mathrm{Fr}_c \leq 0.6$ and is equivalent to an anti-symmetry condition for $\mathrm{Fr}_c \geq 5.0$. An offset exists between the forces predicted

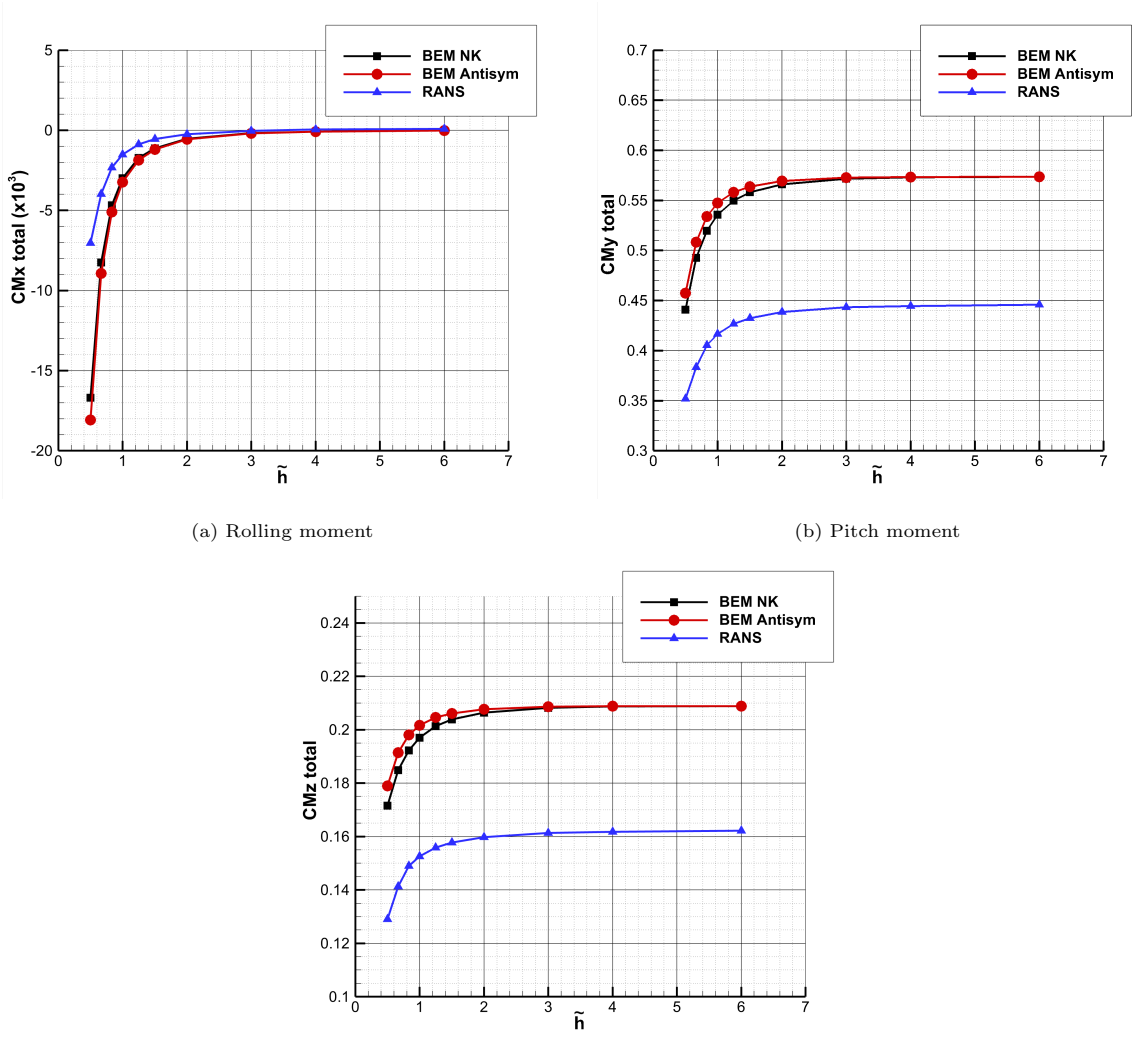

(a) Rolling moment

(b) Pitch moment

(c) Yaw moment

Figure 21: Moment coefficients predicted by the RANS and BEM computations for the two-body configuration ($\mathrm{Fr}_c = 9$). Only the pressure contribution of the forces is used to compute the coefficients.

by the BEM and the RANS computations, due to the boundary layer developing on the hydrofoil in the viscous computations. We believe that this is not related to the linearization of the free surface. Nevertheless, the general variations of the hydrodynamic coefficients with the Froude number are well captured by the "low-fidelity" method. In particular, the lift was found to increase when the submergence depth decreases for $\mathrm{Fr}_c \leq 0.6$, while the opposite behavior was obtained $\mathrm{Fr}_c \geq 0.6$. The free surface predicted by the BEM was in overall good agreement with the "high-fidelity" results, even though the waves amplitudes are slightly overestimated by the potential flow approach. The influence of the submergence depth on the drag and lift coefficients was investigated for a high Froude number $\mathrm{Fr}_c = 9$, typical of real flow conditions.

Despite an offset between the BEM and RANS results, the variations of the forces are in good agreement. The anti-symmetry and Neumann-Kelvin conditions give similar predictions of the forces. For the smallest submergence-to-chord ratio, i.e. $\tilde{h} = 0.83$, the pressure drag and lift decrease by roughly 12% and 25% respectively.

Computations at $\mathrm{Fr}_c = 9$ were performed for the two-body configuration with several submergence depths. The reciprocal influences of the front wing and the stabilizer were first investigated showing a small influence of the stabilizer on the forces acting on the front wing. The presence of the front wing upstream the stabilizer was found to reduce the pressure drag and even switch to a propulsive component of pressure forces on the stabilizer. The presence of the front wing increases the absolute lift of the stabilizer. The Neumann-Kelvin condition was found to provide more accurate force predictions than the anti-symmetry condition for this two-body configuration. Compared to the single wing configuration, larger discrepancies exist between the results using the Neumann-Kelvin condition and the RANS results for the total pressure drag variation with the submergence-to-chord ratio. Nevertheless, both approaches predict a maximum pressure drag around $\tilde{h} = 1$.

It was found that the BEM code is able to provide the main tendencies for the pressure drag and lift variations of a hydrofoil with varying submergence depth and Froude number value. While a day is needed for a typical RANS computation on 32 cpus, a typical BEM simulation is done within a few minutes with a desktop computer. This speed-up represents a significant advantage for the surrogate model construction, allowing to span a vast variety of design solutions. Thus, the potential code could be used to build a "low-fidelity" meta-model, without introducing additional uncertainties on the "high-fidelity" surrogate given by the RANS computations. As future work, the code PUFFIn will be used within an optimization process, to assess the ability of the multi-fidelity surrogate to accurately model inter-level error, as wall as the viscous part of the drag, which is not captured by the potential flow approach. While the use of a low-fidelity solver such as PUFFIn can reduce the computational cost of hydrofoil optimization, several issues were identified by Solak et al. [35] for the optimization procedure. Particularly, when the number of training points becomes important the costs of the adaptive sampling and optimization become significant compared to the potential flow computations. Another issue is data clustering during the adaptive sampling, which may be overcome by a noise filtering procedure. Finally, the solver will be further developed to take into account cavitation effects and to handle surface piercing hydrofoils, since these configurations often occur for windsurfers.

Appendix A. Grid convergence study for the RANS computations

A grid convergence study has been conducted for the RANS computations on the two-body configuration following the procedure presented by Wackers et al. [46]. Five grids have been generated with different threshold values for the Adaptive Grid Refinement (AGR) procedure. For the criterion based on the pressure Hessian the threshold varies between $Th = c_{\text{stab}}$ and $Th = c_{\text{stab}}/16$. For each grid the target cells size at the interface also varies between $Th = c_{\text{stab}}/4 \times 1.2$ and $Th = c_{\text{stab}}/64 \times 1.2$. The mesh used in the present work corresponds to the finer grid. The Froude number is Fr_c=9 and the submergence ratio $\tilde{h} = 0.83$. The method proposed by Eça and Hoekstra [10] is applied to the total hydrodynamic coefficients. The method uses least-squares fits to estimate the error and provides numerical uncertainties. The uncertainties are computed for the three finer grids. As presented in figure A.22, the vertical and side forces are already well converged with the coarsest mesh and the uncertainties are very small (less than 0.5%). An oscillatory convergence is obtained for the drag coefficient C_x^{tot}, leading to larger numerical uncertainties. With the finest mesh, the uncertainties on the hydrodynamic coefficients are $U_{C_x^{\text{tot}}} = 2.9\%$, $U_{C_y^{\text{tot}}} = 0.1\%$ and $U_{C_z^{\text{tot}}} = 0.1\%$, suggesting that the numerical errors are small with the grid used in the present work.

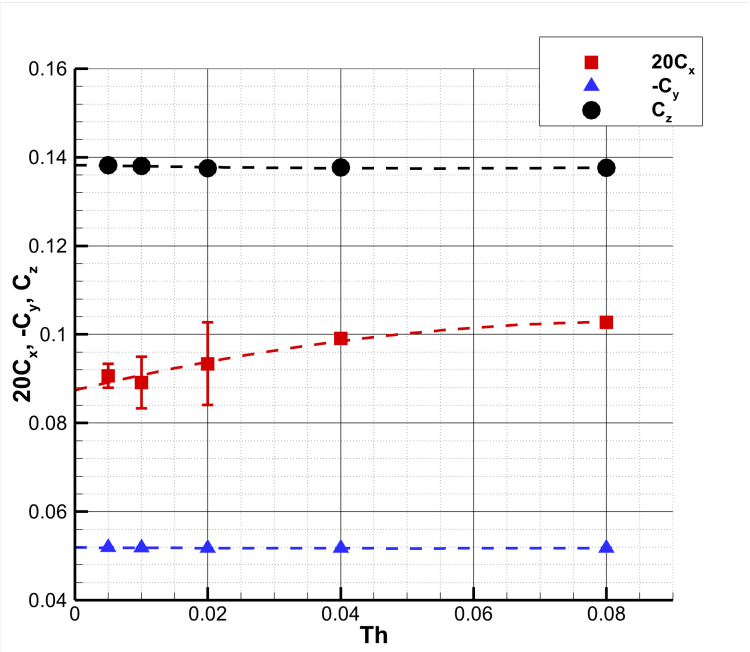

Figure A.22: Grid convergence study for the hydrodynamic coefficients for 5 values of the AGR thresholds. The error bars represent the numerical uncertainties and the dashed line the best polynomial fit obtained with the method of Eça and Hoekstra [10].

Appendix B. Comparison of RANS, Euler and BEM computations

Additional computations have been performed with the solver ISIS-CFD to investigate the influence of the boundary layer on the hydrodynamic coefficients. For these computations the Euler model is used: the viscosity and turbulence effects are neglected in the equations. This way, there is no boundary layer in the Euler simulations and potential flow solutions are expected. The hydrodynamic coefficients predicted by the RANS, Euler and BEM computations for different Froude numbers and $\tilde{h} = 0.83$ are presented in figure B.23 for the front wing. The BEM predictions are in excellent agreement with the results of the Euler computations. The small differences may be due to the free surface condition, since it is linearized in the BEM computations. The coefficients C_y and C_z predicted by the RANS computations are almost 30% smaller than the ones predicted by the Euler model. This suggests that the boundary layer induces a reduction of the effective camber of the foil, resulting in a smaller lift force. Nevertheless, consistent tendencies are predicted by the three models.

References

[1] Ausman, J., 1954. Pressure limitation on the upper surface of a hydrofoil .

[2] Bal, S., 1998. A potential based panel method for 2-d hydrofoils. Ocean Engineering 26, 343–361.

[3] Bal, S., 2007. High-speed submerged and surface piercing cavitating hydrofoils, including tandem case. Ocean Engineering 34, 1935–1946.

[4] Bal, S., 2023. Numerical investigation of curved tip effect on the performance of 3-d cavitating hydrofoils moving under free surface. Journal of Sailing Technology 8, 39–64.

[5] Bal, S., Kinnas, S., 2002. A BEM for the prediction of free surface effects on cavitating hydrofoils. Computational Mechanics 28, 260–274.

[6] Brard, R., 1972. The representation of a given ship form by singularity distributions when the boundary condition on the free surface is linearized. Journal of Ship Research 16, 79–92.

[7] Dawson, C., 1977. A practical computer method for solving ship-wave problems, in: Proceedings of Second International Conference on Numerical Ship Hydrodynamics, pp. 30–38.

[8] Di Mascio, A., Broglia, R., Muscari, R., 2007. On the application of the single-phase level set method to naval hydrodynamic flows. Computers & Fluids 36, 868–886.

[9] Duncan, J., 1981. An experimental investigation of breaking waves produced by a towed hydrofoil. Proceedings of the Royal Society of London. A. Mathematical and Physical Sciences 377, 331–348.

[10] Eça, L., Hoekstra, M., 2014. A procedure for the estimation of the numerical uncertainty of cfd calculations based on grid refinement studies. Journal of computational physics 262, 104–130.

[11] Esmaeilifar, E., Djavareshkian, M., Feshalami, B., Esmaeili, A., 2017. Hydrodynamic simulation of an oscillating hydrofoil near free surface in critical unsteady parameter. Ocean Engineering 141, 227–236.

[12] Faltinsen, O., 2005. Hydrodynamics of high-speed marine vehicles. Cambridge university press.

[13] Filippas, E., Belibassakis, K., 2014. Hydrodynamic analysis of flapping-foil thrusters operating beneath the free surface and in waves. Engineering Analysis with Boundary Elements 41, 47–59.

[14] Filippas, E., Belibassakis, K., 2022. A nonlinear time-domain bem for the performance of 3d flapping-wing thrusters in directional waves. Ocean Engineering 245, 110157.

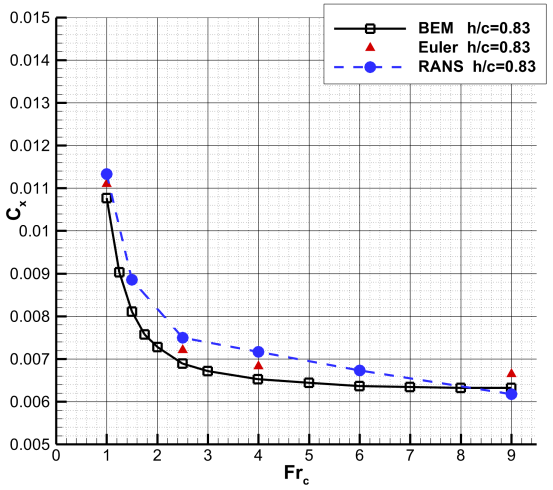

(a) C_x (pressure drag)

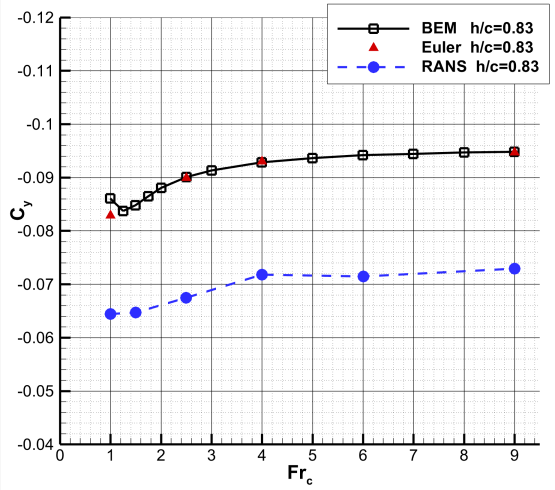

(b) C_y

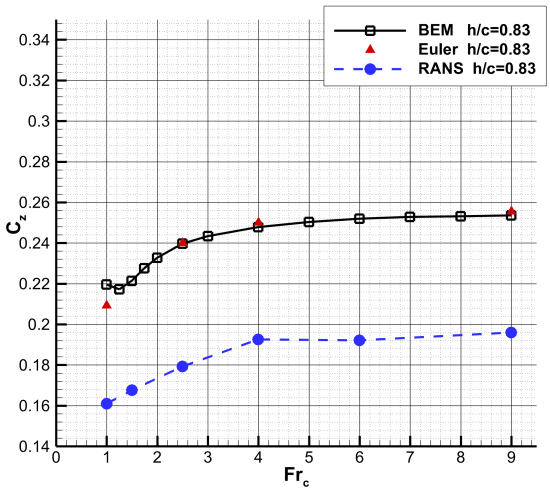

(c) C_z

Figure B.23: Comparison of the hydrodynamic coefficients predicted by the potential code (NK conditions) with the ones predicted by Euler computations for several Froude numbers Fr_c ($\tilde{h} = 0.83$). Only the contributions due to the pressure are used to compute the forces coefficients for both methods.

[15] Forbes, L., 1985. A numerical method for non-linear flow about a submerged hydrofoil. Journal of Engineering Mathematics 19, 329–339.

[16] Gaggero, S., Gonzalez-Adalid, J., Sobrino, M.P., 2016. Design of contracted and tip loaded propellers by using boundary element methods and optimization algorithms. Applied Ocean Research 55, 102–129.

[17] Gennaretti, M., Bernardini, G., 2007. Novel boundary integral formulation for blade-vortex interaction aerodynamics of helicopter rotors. AIAA journal 45, 1169–1176.

[18] Giesing, J., Smith, A., 1967. Potential flow about two-dimensional hydrofoils. Journal of Fluid Mechanics 28, 113–129.

[19] Hess, J., Smith, A., 1964. Calculation of nonlifting potential flow about arbitrary three-dimensional bodies. Journal of

Ship Research 8, 22–44.

[20] Hough, G., Moran, J., 1969. Froude number effects on two-dimensional hydrofoils. Journal of Ship Research 13, 53–60.

[21] Karim, M., Prasad, B., Rahman, N., 2014. Numerical simulation of free surface water wave for the flow around NACA 0015 hydrofoil using the volume of fluid (VoF) method. Ocean Engineering 78, 89–94.

[22] Katz, J., Plotkin, A., 2001. Low-speed aerodynamics. volume 13. Cambridge university press.

[23] Keldysch, M., Lawrentjew, M., 1935. On the motion of a wing below the surface of a heavy fluid. ZAHI paper, (Jan. 1935) Moscow.

[24] Kennell, C., Plotkin, A., 1984. A second-order theory for the potential flow about thin hydrofoils. Journal of Ship Research 28, 55–64.

[25] Kutta, W., 1902. Auftriebskräfte in strömenden Flüssigkeiten. Illustrierte Aeronautische Mitteilungen 6, 133–135.

[26] Lachaume, C., Biausser, B., Fraunié, P., Grilli, S., Guignard, S., 2003. Modeling of breaking and post-breaking waves on slopes by coupling of BEM and VoF methods, in: The Thirteenth International Offshore and Polar Engineering Conference, OnePetro.

[27] Leroyer, A., Wackers, J., Queutey, P., Guilmineau, E., 2011. Numerical strategies to speed up CFD computations with free surface—application to the dynamic equilibrium of hulls. Ocean Engineering 38, 2070–2076.

[28] Longuet-Higgins, M., Dommermuth, D., 1997. Crest instabilities of gravity waves. part 3. Nonlinear development and breaking. Journal of Fluid Mechanics 336, 33–50.

[29] Menter, F., Kuntz, M., Langtry, R., 2003. Ten years of industrial experience with the SST turbulence model. Turbulence, Heat and Mass Transfer 4, 625–632.

[30] Menter, F., Langtry, R., 2012. Transition modelling for turbomachinery flows. Low Reynolds Number Aerodynamics and Transition , 31–58.

[31] Molland, A., 2011. The maritime engineering reference book: a guide to ship design, construction and operation. Elsevier.

[32] Nakos, D., Sclavounos, P., 1990. On steady and unsteady ship wave patterns. Journal of Fluid Mechanics 215, 263–288.

[33] Newman, J., 2018. Marine hydrodynamics. The MIT press.

[34] Ni, Z., Dhanak, M., Su, T., 2019. Performance of a slotted hydrofoil operating close to a free surface over a range of angles of attack. Ocean Engineering 188, 106296.

[35] Pehlivan Solak, H., Wackers, J., Pellegrini, R., Serani, A., Diez, M., Perali, P., Sacher, M., Leroux, J.B., Augier, B., Hauville, F., et al., 2023. Hydrofoil optimization via automated multi-fidelity surrogate models, in: 10th International Conference on Computational Methods in Marine Engineering (MARINE 2023).

[36] Pellegrini, R., Wackers, J., Broglia, R., Serani, A., Visonneau, M., Diez, M., 2022. A multi-fidelity active learning method for global design optimization problems with noisy evaluations. Engineering with Computers , 1–24.

[37] Perali, P., 2023. Puffin documentation. `https://www.ensta-bretagne.fr/fr/optifoil`.

[38] Pernod, L., Sacher, M., Wackers, J., Augier, B., Bot, P., 2023. Free-surface effects on two-dimensional hydrofoils by RANS-VoF simulations. Journal of Sailing Technology 8, 24–38.

[39] Plotkin, A., 1975. The thin-hydrofoil thickness problem including leading-edge corrections. Journal of Ship Research 19, 122–129.

[40] Prasad, B., Hino, T., Suzuki, K., 2015. Numerical simulation of free surface flows around shallowly submerged hydrofoil by OpenFOAM. Ocean Engineering 102, 87–94.

[41] Queutey, P., Visonneau, M., 2007. An interface capturing mandhod for free-surface hydrodynamic flows. Computers & Fluids 36, 1481–1510.

[42] Richeux, J., 2022. Towards the automation of adaptive RANS simulations for hydrofoils. Master's thesis. Ecole Centrale de Nantes.

[43] Sacher, M., Le Maitre, O., Duvigneau, R., Hauville, F., Durand, M., Lothodé, C., 2021. A non-nested infilling strategy

for multifidelity based efficient global optimization. International Journal for Uncertainty Quantification 11.

[44] Serani, A., Stern, F., Campana, E., Diez, M., 2022. Hull-form stochastic optimization via computational-cost reduction methods. Engineering with Computers 38, 2245–2269.

[45] Wackers, J., Deng, G., Guilmineau, E., Leroyer, A., Queutey, P., Visonneau, M., 2014. Combined refinement criteria for anisotropic grid refinement in free-surface flow simulation. Computers & Fluids 92, 209–222.

[46] Wackers, J., Deng, G., Guilmineau, E., Leroyer, A., Queutey, P., Visonneau, M., Palmieri, A., Liverani, A., 2017. Can adaptive grid refinement produce grid-independent solutions for incompressible flows? Journal of Computational Physics 344, 364–380.

[47] Wackers, J., Koren, B., Raven, H.C., Van der Ploeg, A., Starke, A., Deng, G., Queutey, P., Visonneau, M., Hino, T., Ohashi, K., 2011. Free-surface viscous flow solution methods for ship hydrodynamics. Archives of Computational Methods in Engineering 18, 1–41.

[48] Xie, N., Vassalos, D., 2007. Performance analysis of 3d hydrofoil under free surface. Ocean Engineering 34, 1257–1264.

[49] Xu, G., Wu, G., 2013. Hydrodynamics of a submerged hydrofoil advancing in waves. Applied Ocean Research 42, 70–78.

[50] Xue, M., Xü, H., Liu, Y., Yue, D., 2001. Computations of fully nonlinear three-dimensional wave–wave and wave–body interactions. Part 1. dynamics of steep three-dimensional waves. Journal of Fluid Mechanics 438, 11–39.

[51] Yeung, R., Bouger, Y., 1979. A hybrid integral-equation method for steady two-dimensional ship waves. International Journal for Numerical Methods in Engineering 14, 317–336.

[52] Zhang, W., el Moctar, O., Schellin, T.E., 2020. Numerical simulations of a ship obliquely advancing in calm water and in regular waves. Applied Ocean Research 103, 102330.